UNIVERSITAT POLITÈCNICA DE VALÈNCIA

_ TELECOM ESCUELA TÉCNICA VLC SUPERIOR DE INGENIERÍA DE TELECOMUNICACIÓN

High-Performance Polarization-Independent Grating Couplers Enabled by Dielectric Metamaterials and Nature-Inspired Algorithms

Jorge Parra Gómez

Supervisor:
Prof. Dr. Pablo Sanchis Kilders

Máster en Ingeniería de Telecomunicación

Escuela Técnica Superior en Ingenieria de Telecomunicación

2019-2020

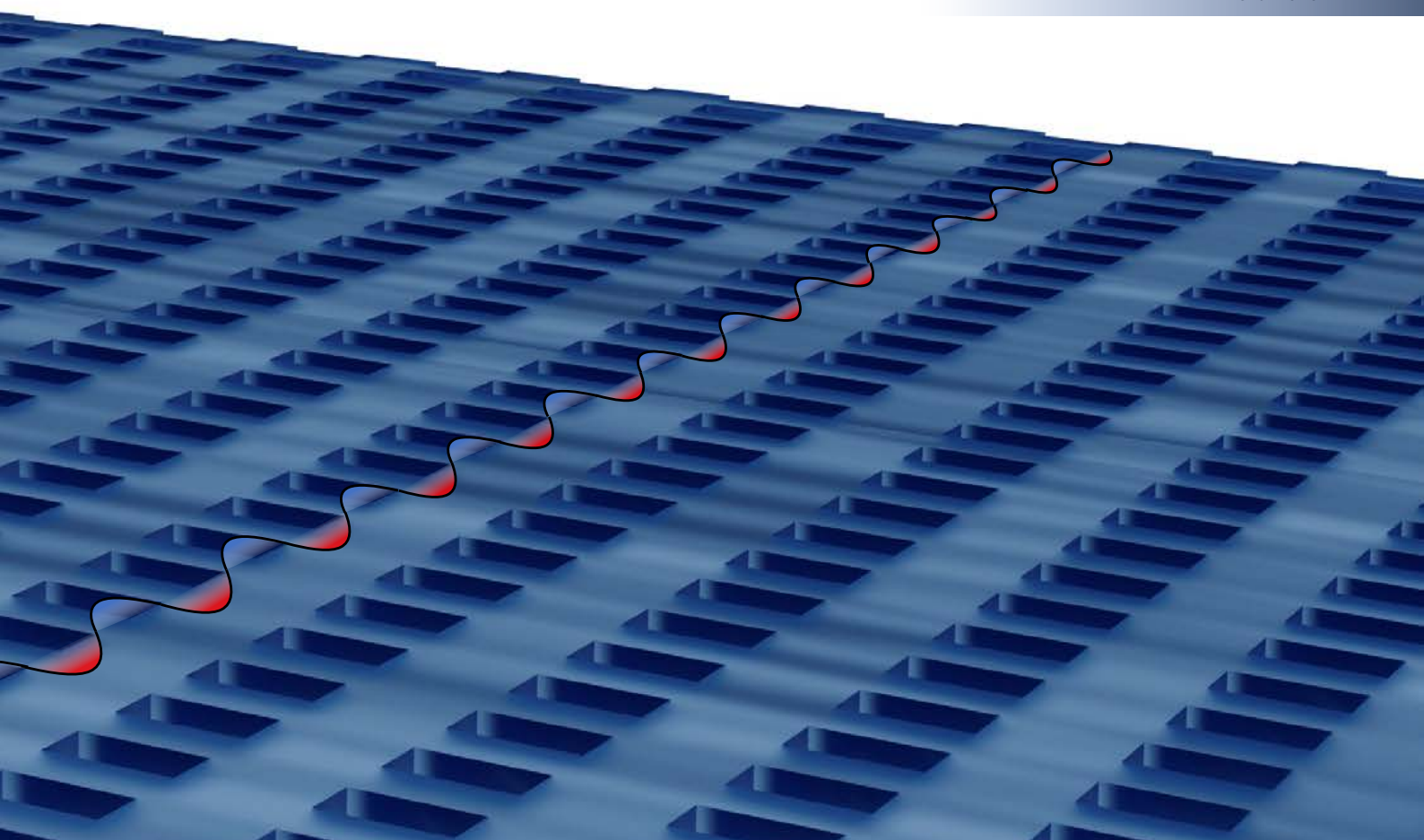

UNIVERSITAT POLITÈCNICA DE VALÈNCIA

TELECOM ESCUELA TÉCNICA VLC SUPERIOR DE INGENIERÍA DE TELECOMUNICACIÓN

High-Performance Polarization-Independent Grating Couplers Enabled by Dielectric Metamaterials and Nature-Inspired Algorithms

Jorge Parra Gómez

Supervisor: Prof. Dr. Pablo Sanchis Kilders

Master Thesis presented at Escuela Técnica Superior de Ingenieros de Telecomunicación of Universitat Politècnica de València, for the fulfillment of the degree of Máster en Ingeniería de Telecomunicación

Academic year 2019-20

Valencia, April 2, 2020

"The best thesis is a finished thesis."

— Anonymous

Agradecimientos

Las primeras líneas de agradecimiento no pueden ir a otra persona que no sea mi tutor Pablo. Gracias por haberme dado la libertad y confianza de realizar y confeccionar este trabajo en base a mi criterio y por dejarme adentrar en "terrenos pantanosos" en los que muchas veces tienes que hacer un salto de fe. Todavía recuerdo que esto comenzó con tu frase "Estaría bien enviar algo al ECIO de este año..." y a mi cabeza no sé porqué se le ocurrió combinar metamateriales dieléctricos con método de optimización basado en algoritmos naturales. Es un lujo haberte tenido como tutor de TFM y que seas mi actual director de tesis.

Gracias a mi familia por haber sido paciente –sobre todo mi madre– con la entrega de este TFM. La espera creo que no ha sido un vano ya que otro máster y una tesis se interpusieron en mi camino. Cuando parecía que había un hueco para terminar este trabajo, surgía un proyecto, una conferencia o la posibilidad de enviar un artículo a revista. Parece ser que técnicamente he tenido que terminar la tesis para poder decir que soy Ingeniero de Telecomunicación con todas las letras y competencias.

Gracias Lilian por haberme enseñado que tan importante es desarrollar una carrera profesional como una personal. Y gracias a compañeros, amigos y a todas las personas que han tenido un gesto de interés por este trabajo.

Resumen

La complejidad de las estructuras emergentes en fotónica integrada hace que su optimización sea difícil y con altos costes asociados en términos de tiempo y recursos. Los circuitos fotónicos integrados (PICs, en inglés) se están convirtiendo en una solución tecnológica para abordar problemas críticos en el campo de las telecomunicaciones, biofotónica o computación cuántica. Específicamente, la fotónica de silicio sobresale como la plataforma mas prometedora para abordarlos. Obtener un proceso de optimización eficiente sería muy codiciado por las compañías para reducir los costes del PIC o proporcionar nuevas y mejores funcionalidades.

En este trabajo, nos ponemos como objetivo probar el potencial de un algoritmo inspirado en la naturaleza como es la optimización por enjambre de partículas (PSO, en inglés) aplicado a estructuras fotónicas. Específicamente, PSO es aplicado para obtener alto prestaciones en redes de difracción insensibles a la polarización para acoplo fibra a PIC. La condición de insensibilidad a la polarización es difícil de obtener en fotónica de silicio debido al gran contraste de índice. Para conseguir esta condición en una red de difracción, la solución mas prometedora es el uso de estructuras sub-longitud de onda que actúan como un metamaterial dieléctrico uniaxial. Como consecuencia, la inclusión de estas estructuras incrementa exponencialmente el número de variables de diseño, lo cual dificulta el uso de procesos estándares de optimización.

En este trabajo, las estructuras sub-longitud de onda son en primer lugar analizadas rigurosamente mediante el método de transferencia de matrices (TMM, en inglés), la expansión modal y la técnica de adaptación modal para determinar bajo que condiciones estas actúan como un material homogéneo. A continuación, la optimización de las redes de difracción insensibles a la polarización es llevada a cabo mediante el desarrollo de un programa que se integra con un software de simulación fotónica (RSoft). El potencial de PSO aplicado a este tipo de estructuras es demostrado requiriendo al algoritmo diferentes especificaciones para la red de difracción.

Los resultados muestran para las estructuras sub-longitud de onda un periodo mínimo de 100 nm a fin de aplicar la aproximación de homogeneidad de forma precisa. Por otra parte, los diseños dados por PSO presentan un alto prestaciones junto con un comportamiento insensible a la polarización comparable al estado del arte. Además, se también se consigue una reducción drástica en el tiempo de optimización en comparación con las técnicas comunes.

De esta forma, PSO se presenta como una herramienta eficiente para optimizar estructuras fotónicas complejas. Estos resultados podrían llamar la atención de la industria de los PIC para reducir sus costes. Por otra parte, los diseños propuestos podrían ser de interés para desarrollar nuevas aplicaciones en el campo de las telecomunicaciones o nuevas formas de computación.

Resum

La complexitat de les estructures emergents en fotònica integrada fa que la seua optimització sigua difícil i amb alts costos associats en termes de temps i recursos. Els circuits fotònics integrats (PICs, en anglès) s'estan convertint en una solució tecnològica per tal d'abordar problemes crítics en el camp de les telecomunicacions, biofotònica o computació quàntica. Específicament, la fotònica de silici sobresurt com la plataforma més prometedora per tal d'abordar-los. Obtenir un procés d'optimització eficient seria molt cobejat per les companyies per reduir els costos del PIC o proporcionar noves i millors funcionalitats.

En aquest treball, ens posem com a objectiu provar el potencial d'un algoritme inspirat en la natura com és l'optimització per eixam de partícules (PSO, en anglès) aplicat a estructures fotòniques. Específicament, PSO és aplicat per obtenir altes prestacions en xarxes de difracció insensibles a la polarització per acoblament fibra a PIC. La condició d'insensibilitat a la polarització és difícil d'obtenir en fotònica de silici a causa del gran contrast d'índex. Per tal d'aconseguir aquesta condició en una xarxa de difracció, la solució més prometedora és l'ús d'estructures sub-longitud d'ona que actuen com un metamaterial dielèctric uniaxial. Com a conseqüència, la inclusió d'aquestes estructures incrementa exponencialment el nombre de variables de disseny, la qual cosa dificulta l'ús de processos estàndards d'optimització.

En aquest treball, les estructures sub-longitud d'ona són en primer lloc analitzades rigorosament mitjançant el mètode de transferència de matrius (TMM, en anglès), l'expansió modal i la tècnica d'adaptació modal amb l'objecte de determinar sota quines condicions aquestes actuen com un material homogeni. A continuació, l'optimització de les xarxes de difracció insensibles a la polarització és porta a terme mitjançant el desenvolupament d'un programa que s'integra amb un programari de simulació fotònica (RSoft). El potencial d'PSO aplicat a aquest tipus d'estructures és demostrat requerint a l'algoritme diferents especificacions per a la xarxa de difracció.

Els resultats mostren per les estructures sub-longitud d'ona un període mínim de 100 nm per tal d'aplicar l'aproximació d'homogeneïtat de forma precisa. D'altra banda, els dissenys donats per PSO presenten unes altes prestacions juntament amb un comportament insensible a la polarització comparable a l'estat de l'art. A més, també s'aconsegueix una reducció dràstica en el temps d'optimització en comparació amb les tècniques comunes.

D'aquesta manera, PSO es presenta com una eina eficient per tal d'optimitzar estructures fotòniques complexes. Aquests resultats podrien cridar l'atenció de la indústria dels PIC per tal de reduir els seus costos. D'altra banda, els dissenys proposats podrien ser d'interès per a desenvolupar noves aplicacions en el camp de les telecomunicacions o noves formes de computació.

Abstract

The complexity of emerging photonic integrated structures makes their optimization difficult and with high associated costs in terms of time and resources. Photonic integrated circuits (PICs) are becoming a technology solution to address some critical problems in the field of telecom, biophotonics or quantum computing. Specifically, silicon photonics stand as the most promising platform to tackle them. Obtaining an efficient optimization process would be desired for companies to reduce the cost of the PIC or provide new and better functionalities.

In the present work, we aim to prove the potential of a nature-inspired algorithm such as particle swarm optimization (PSO) applied to photonic structures. Specifically, PSO is applied for obtaining high-performance in polarization-insensitive grating couplers for fibre-to-PIC coupling. The polarization-intensive condition is hard to achieve in silicon photonics due to the large index contrast. To achieve this condition in grating couplings the most promising solution is the utilization of subwavelength structures that act as a uniaxial dielectric metamaterial. As a consequence, the inclusion of these structures increases exponentially the number of design variables, which difficult the utilization of standard optimization processes.

In this work, the subwavelength structures are first rigorously analysed by using transfer matrix method (TMM), eigenmode expansion and mode-matching to determine under which conditions these act as a homogenous material. Afterwards, the optimization of polarization-insensitive grating couplers is carried out by developing a program that integrates with a photonic simulation software (RSoft). The potential of PSO applied to this kind of structure is demonstrated by demanding different grating specifications to the algorithm.

Results show for the subwavelength structures a minimum pitch of 100 nm in order apply accurately the homogenous approximation. On the other hand, the designs given by PSO present high-performance together with a polarization-insensitive behaviour comparable to the state-of-the art. Furthermore, a drastic reduction of the optimization time in comparison with common techniques is also achieved.

Hence, PSO presents as an efficient tool for optimizing complex photonic structures. These results could catch the attention of the PIC industry to implement this cost-savings. Furthermore, the proposed designs could be of interest for developing new applications in the field of telecom or new ways of computing.

Contents

Chapter 1

Introduction

1.1 Context and Motivation

As well as electronics revolutionized the last century, photonics is becoming the most suitable technology to face current and forthcoming humanity's challenges. Among them, data growths year after year [1, 2]. Light can address this problem by encoding the information in its enormous bandwidth [3,4]. Currently, optical communications are mainly based on mature technologies such as fibre optics and discreet components (laser, photodiodes, modulators...). However, the need of reducing costs, produce very large-scale integration (VLSI) or implement multi-functions can only be fulfilled by using photonic integrated circuits (PICs) [5].

PICs can be developed in a wide variety of platforms, and among them, silicon photonics is the most versatile due to the excellent electronic/optical integration and the ultra-small size of the cross-section waveguides [6, 7]. On one hand, the electro-optic integration is enabled by the CMOS-compatibility (complementary-metal-oxide-semiconductor) platform which benefits of mature and well-established fabrications processes of micro- and nano-electronic industry. On the other hand, the high refractive index contrast allows to confine the light in the nanoscale. As a result, silicon photonics has wakened the interest of industry in the recent years with a market growing exponentially as reported by Yole [8]. For instance, the silicon photonics-based transceiver is forecasted to achieve $4 billion in 2024 (see Fig. 1.1).

In the research field, silicon photonics stands as the preferred platform for developing disruptive and ground-breaking topics such as integrated quantum photonics [9], neuromorphic photonics [10] or seamless integration of photonics with nanoelectronics [11] (see Fig. 1.2).

However, despite the silicon photonics technology is beyond the tipping point, it is not yet fully mature and cannot be compared with the maturity of fibre-based optical communications. Indeed, some topics such as the fibre-to-chip coupling should be addressed. Due to the large cross-section mismatch between an optical fibre ($\sim$ 300 μm^2) and the silicon waveguide of a PIC ($\sim$ 0.11 μm^2), direct coupling them implies very high optical losses. To address this drawback, a coupling structure that act as an interface should be used. Several coupling strategies have been proposed based either in edge coupling or vertical coupling. In the first case, the light is coupled by placing the fibre and the waveguide in the same plane (Fig. 1.3a). In the latter, the fibre is placed vertical to the top surface of the PIC and the light beam is focused to the silicon waveguide by

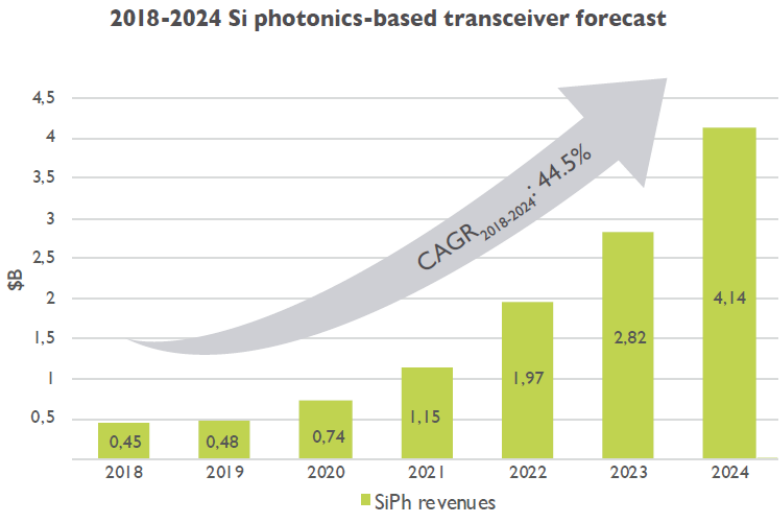

Figure 1.1. Silicon photonics-based transceiver forecast [8].

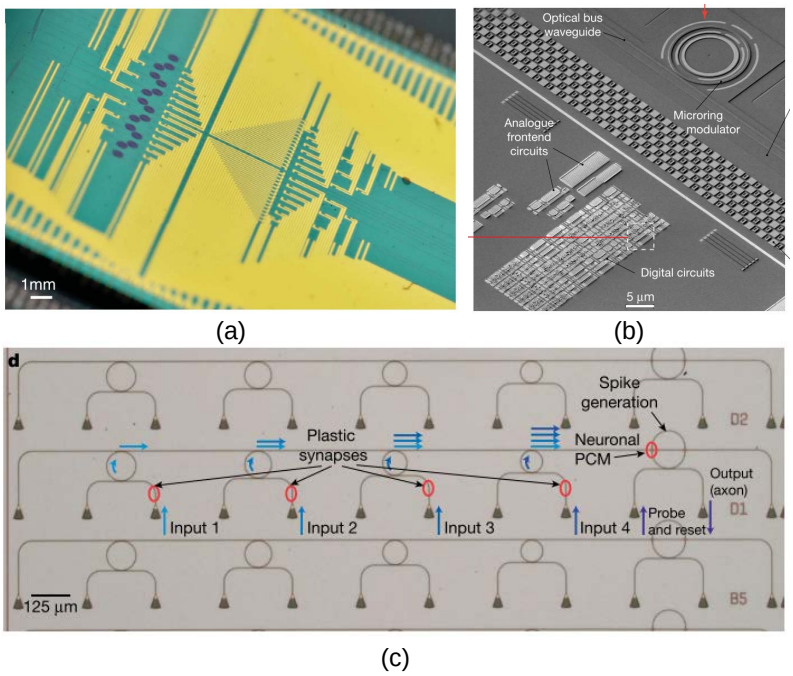

Figure 1.2. **(a)** Integrated quantum photonic circuit [9]. **(b)** Photonic circuit with electronics in the same chip [11]. **(c)** All-optical neural network based on micro-ring resonators and phase-change materials [10].

using a diffractive grating known as grating coupler (Fig. 1.3b).

Although edge coupling approaches may provide low optical losses, grating couplers stand as the most popular solution due to several factors: (i) the structure integrates seamless in the PIC; (ii) grating couplers can be placed in any point of the chip, which facilitates testing at wafer-level structure; and (iii) they have higher alignment tolerances compared to the edge coupling approaches.

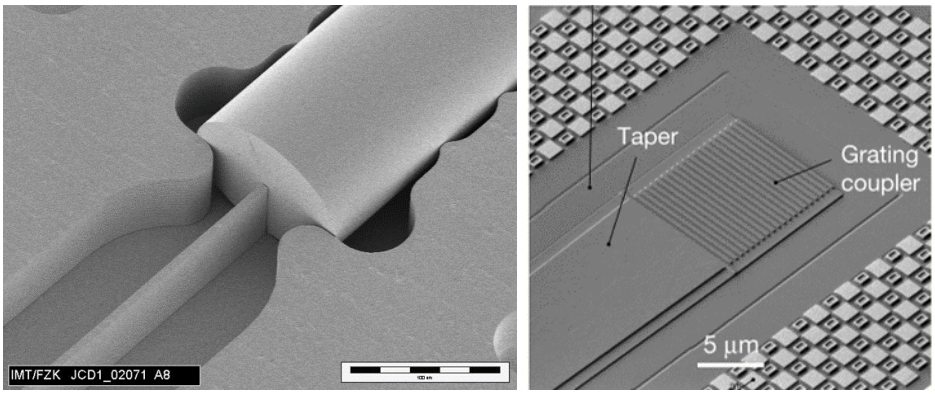

(a) **(b)**

Figure 1.3. Fibre-to-PIC coupling strategies: **(a)** Edge-coupler [12] and **(b)** grating coupler [11].

However, grating couplers suffer from high polarization dependence loss (PDL) because their strong birefringence and thus, a control polarization stage out of the chip is required before injecting the light into the PIC. The randomness in which arrives the light to the PIC due to external factors such as fibre bending implies a problem in terms of optical losses, eliminates the possibility of using on-chip polarization-division multiplexing [13] and increases the cost of the optical system because of the out-of-chip polarization stage.

Therefore, polarization-independent grating couplers for the silicon photonics platform and working at telecom wavelengths are highly desirable. In this context, some approaches based on polarization diversity have been proposed in which the grating coupler can be viewed as a superposition of two gratings [14] (see Fig. 1.4). However, the on-chip light is polarized only along a certain axis and usually there is a need to replicate the structures comprising the PIC. Hence, one-dimensional polarization-independent grating couplers that maintain the input polarization into the PIC are highly appeal.

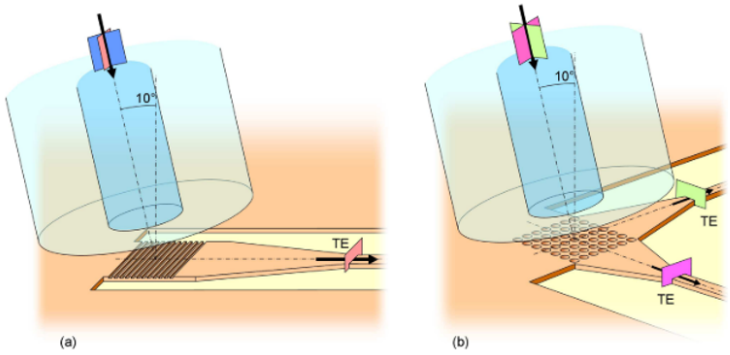

Figure 1.4. Polarization diversity grating coupler [14].

1.2 State-of-the-art

One-dimensional polarization-independent grating couplers have been proposed relying on different techniques such as using of subwavelength (SWG) structures [15, 16] (see Fig. 1.5), geometrical intersection of two different uniform grating couplers [17] or exploiting different diffraction orders modes [18]. Among all, the utilization of subwavelength structures has delivered the best performance (see Table 1.1 and sections 4.1 and 4.2.2 for definitions). Furthermore, this kind of gratings benefit of an easier fabrication process since are fabricated using the same full-etch step of the waveguides instead of the typical two-steps of standard gratings.

Table 1.1. One-dimensional polarization-independent grating couplers comparison. CE = Coupling efficiency, PDL = Polarization dependence loss, BW = Bandwidth and WG = Waveguide.

Ref.	Exp.	Method	TE-CE (dB)	TM-CE (dB)	PDL (dB)	PDL BW (nm)	Wavelength (nm)	WG thickness (nm)
[15]	No	SWG (400 nm)	-4	-4	~ 0	80 nm	1550	340
[16]	Yes	SWG (400 nm)	-3.2	-4.3	~ 0.2	12 nm	1460/1510	340
[17]	Yes	TE/TM intersection	-7.8	-8	~ 0.2	20 nm	1550	220
[18]	No	TE_{00}/TM_{10} coupling	-3	-3	~ 0	30 nm	1550	400

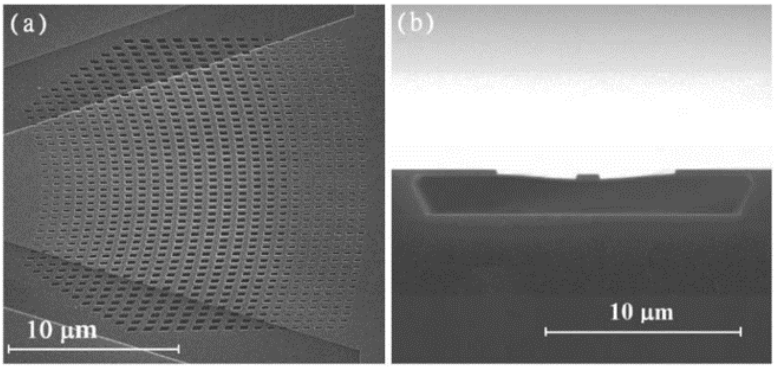

Figure 1.5. Suspended polarization-independent grating coupler based on subwavelength structures [16].

However, the inclusion of another structure increases the degrees of freedom and difficulties to obtain the best design through laborious and non-efficient optimization process. The low-efficient design process can suppose an increase in the cost of the PIC. Hence, efficient design strategies with a wide application range may be highly alluring for the industry.

1.3 Project Outline

The present master thesis is comprised from 5 chapters and 3 appendices. The appendices are also work that has been developed throughout this thesis but are not included

in the main text to not break the pace of the reader. These are mainly theoretical developments and simulation methods. Thus, the organization of this thesis is as follows:

- **Chapter 1: Introduction**: The first chapter deals with motivation and problem statement of this work. The state-of-the art about polarization-independent grating couplers is reviewed.
- **Chapter 2: Objectives**: In this chapter main objectives of the present thesis are outlined.
- **Chapter 3: Methodology**: The project management, work packages in which is divided the work and temporal distribution are addressed.
- **Chapter 4: Development and Results**: This chapter is the core of the present work. The structures and algorithms in which rely the designed polarization-insensitive grating couplers are analysed and implemented: (i) subwavelength structures and (ii) particle swarm optimization algorithm. The aim of this chapter is two-fold. First, crucial design parameters are set based on rigorous simulations. The simulation methods used to derive these values are explained in the appendices. Second is to present the performance of the gratings based on the aforementioned design parameters.
- **Chapter 5: Conclusions and Future Work**: In this chapter main conclusions and implications are stated. Furthermore, future prospects and concluding remarks are outlined.
- **Author's Merits**: Summarised the main contributions related to this work that have been published.
- **Bibliography**: Lists the referenced works in order of appearance.
- **Appendix A: Numerical Simulation Methods**: This appendix explains and justifies the main parameters used for simulations based on finite element methods and finite-difference time-domain.
- **Appendix B: Transfer Matrix Method for Periodic Structures**: The field profile expression and the associated effective refractive index in a periodic structure is derived by means of the transfer matrix method.
- **Appendix C: Eigenmode Expansion and Mode-Matching**: This last appendix describes the eigenmode expansion and mode-matching technique applied to the interface of a homogenous medium and a periodic structure. Electromagnetic parameters such as reflectance and transmittance are also derived for this case.

Chapter 2

Objectives

In the present work, we investigate the utilization of nature-inspired algorithms such as particle swarm optimization (PSO) for efficient optimization of polarization-independent grating couplers based on dielectric metamaterials. The main objective is to achieve a performance comparable to those reported state-of-the-art with a drastic decrease in the optimization process. Detailed objectives of the present work are listed as follows:

- Demonstrate the feasibility of nature-inspired algorithms for efficient design of complex photonic integrated structures with performance comparable to the state-of-the-art.
- Integrate a nature-inspired algorithm such as PSO in a photonic design commercial software such as RSoft.
- Determine under which conditions periodic subwavelength structures can act as a dielectric metamaterial for enabling polarization-independency of grating couplers.
- Determine the optimum thickness of the grating coupler waveguide for achieving polarization-independence performance.
- Investigate the definition of the most suitable figure of merit in terms of the achieved optimum design.

Chapter 3

Methodology

3.1 Project Management

The present work tries to be ambitious in the sense of involving several different topics such as algorithms, advanced electromagnetism, numerical simulation methods or programming with the aim of facilitating the design procedure of advanced photonic structures. The utilization of these topics in an emerging field such as silicon photonics or the utilization of new discipline such as subwavelength integrated photonics arise problems that must be addressed most of the times with a lack of information in the literature. For instance, regarding the PSO algorithm, their optimization parameters are well-known to be problem dependent and, up to date, the use of PSO has not been reported for the kind of structure used in this work. Basing on our simulations, the subwavelength structures that enable the polarization-independence condition require of a more exhaustive investigation compared to the works previously reported. Finally, the programming part needs to deal an exhaustive debug procedure because of the integration with a commercial software.

This work started with an initial proof-of-concept that was presented at the 19^{th} European Conference on Integrated Optics (ECIO) as an oral talk [19]. Despite the successful demonstration of PSO for polarization-independent grating couplers, there were some open questions that could not be addressed at that moment. Some discrepancies where observed between 2D and 3D simulations with their origin to be determined. Furthermore, the integration of the PSO algorithm with the commercial software was very basic. In this work, open questions are tried to be addressed with a solid response and integration of the PSO algorithm is achieved with fully transparency to the designer using a user-friendly interface.

3.2 Work Packages

In contrast to the "traditional, sequential approach" based on the consecution of "work packages", here we propose a disruptive methodology based on the Agile Scrum framework. Scrum is an iterative and incremental agile development framework in which the consecution of the project is based in cycles inspired by empirical inspect and adapt feedback loops to cope with complexity and risk. The main packages and sub-packages are listed as follows and their interdependence is depicted in Fig. 3.1. As it can be

noticed, work packages 2 and 3 are interdependent and they feed back.

1. **Review literature**
   (a) Grating couplers
      i. Polarization-independent
   (b) Subwavelength periodic structures
      i. Crosswise structures
   (c) Nature-inspired algorithms
      i. Particle swarm optimization
2. **Determine the conditions of using a crosswise periodic structure as a metamaterial with a homogenous uniaxial dielectric response**
   (a) Study of its dispersion-relation equation.
   (b) Analyse the field profile of the structure.
   (c) Analyse the transmittance and reflectance values when the subwavelength structure is interfaced with a homogenous material.
3. **Develop the PSO algorithm for polarization-independent grating couplers**
   (a) Determine the most optimal PSO parameters such as the inertia weight, social and cognitive coefficients, etc.
   (b) Define the figure(s) of merit.
   (c) Develop a computer program in C# that integrates with the commercial software of RSoft suite.
4. **Write final report**

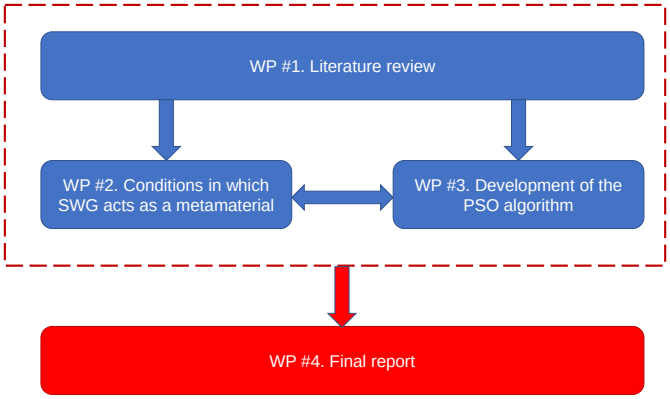

Figure 3.1. Work packages diagram.

3.3 Temporal Distribution

The temporal distribution of the work packages is shown in the following Gantt diagram. Due to the nature of work package #1, this is transverse to the full development of the work. Second and third work packages are developed simultaneously in order to cope with complexity and risk because its interdependence. Finally, the last work package deals with the reporting of the obtained results highlighting the main achieved conclusions and future work.

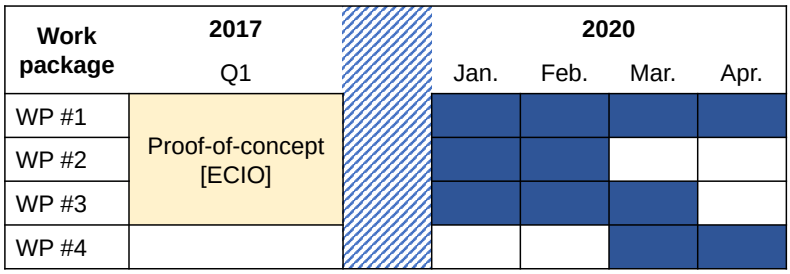

Figure 3.2. Work packages diagram.

Chapter 4

Development and Results

4.1 Background and Formalism

Before delving into the core of this work, it is important to address some clarifications about a few terms such as polarization, material properties or effective refractive index that are used throughout this work.

Polarization

The polarization can be defined as transverse-electric (TE) or transverse-magnetic (TM) depending on which are the main components of the electric (**E**) and magnetic (**H**) field. For a wave propagating in the z-axis, the components of both fields depending on the light confinement and can be classified as follows:

- No confinement [Free space (Fig. 4.1a)]:
  - TE: **E** = $\{E_x, 0, 0\}$ and **H** = $\{0, H_y, 0\}$.
  - TM: **E** = $\{0, E_y, 0\}$ and **H** = $\{H_x, 0, 0\}$.
- One-dimension [Slab waveguide (Fig. 4.1b)]:
  - TE: **E** = $\{E_x, 0, E_z\}$ and **H** = $\{0, H_y, 0\}$.
  - TM: **E** = $\{0, E_y, 0\}$ and **H** = $\{H_x, 0, E_z\}$.
- Two-dimensions [Strip waveguide (Fig. 4.1c)]:
  - TE: **E** = $\{E_x, E_y, E_z\}$ and **H** = $\{H_x, H_y, H_z\}$.
  - TM: **E** = $\{E_x, E_y, E_z\}$ and **H** = $\{H_x, H_y, H_z\}$.

In a strip waveguide, **E** and **H** fields are not fully transverse though the major part of the E-field is comprised in the x-axis (TE) or y-axis (TM).

The effective refractive index

The field distribution of a wave, $\boldsymbol{\phi}$, travelling through the z-axis can be expressed as:

$$\boldsymbol{\phi}(x, y, z) = \boldsymbol{\phi}(x, y) \exp\left(-j\frac{2\pi}{\lambda_{eff}}z\right) \tag{4.1}$$

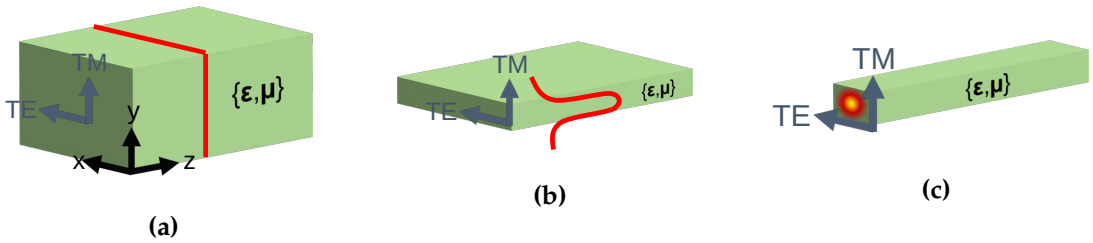

Figure 4.1. Illustration of the E-field for the different field confinement: **(a)** Free space, **(b)** slab waveguide and **(c)** strip waveguide.

where $\boldsymbol{\phi} = \{\phi_x, \phi_y, \phi_z\}$ and stands for the **E**- or **H**-field. The term λ_{eff} refers to the effective wavelength that is defined as:

$$\lambda_{eff} = \frac{\lambda}{n_{eff}} \tag{4.2}$$

where λ is the wavelength in the vacuum and n_{eff} is the so-called effective refractive index. This latter depends on several aspects such as the geometry of the medium in which the light propagates, the optical properties of the materials that comprises the medium, i.e., the permeability, $\boldsymbol{\mu}$, and permittivity, $\boldsymbol{\varepsilon}$, and the working wavelength. Obtaining the value of n_{eff} from Maxwell's equations in 1D or 2D structures is not straightforward since no analytical solution exists. Hence, numerical simulators based, for instance, on finite element method (FEM) are required.

On the other hand, in this thesis, two types of waves are obtained depending on whether n_{eff} is a pure real or imaginary number (see Fig. 4.2). From Eq. (4.1) if n_{eff} is real then the exponential is complex, and the light propagates. Conversely, if n_{eff} is imaginary, the exponential is real and the amplitude of the light decays with the z-axis referred as leaky waves. Moreover, the number of real solutions is finite and usually a single solution is desired (single-mode condition), whereas the number of leaky waves is infinite.

Material's optical properties

Both permeability and permittivity are defined as:

$$\boldsymbol{\mu} = \mu_0 \boldsymbol{\mu_r} \tag{4.3}$$

$$\boldsymbol{\varepsilon} = \varepsilon_0 \boldsymbol{\varepsilon_r} \tag{4.4}$$

where μ_0 and ε_0 are the vacuum permeability and permittivity, respectively, and $\boldsymbol{\mu_r}$ and $\boldsymbol{\varepsilon_r}$ are the relative permeability and permittivity tensors, respectively. From these latter, the refractive index of the medium is obtained as $\boldsymbol{n} = \sqrt{\boldsymbol{\varepsilon_r}\boldsymbol{\mu_r}}$. Usually, PICs are based on dielectric materials with non-magnetic response ($\mu_r = 1$). Furthermore, in the present work we will deal as most with uniaxial homogenous linear (UHL) materials, thus:

$$\boldsymbol{\varepsilon_r} = \begin{pmatrix} \varepsilon_{xx} & 0 & 0 \\ 0 & \varepsilon_{yy} & 0 \\ 0 & 0 & \varepsilon_{zz} \end{pmatrix} \tag{4.5}$$

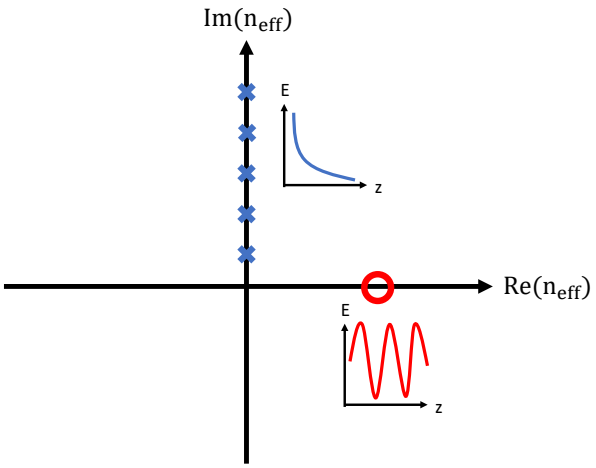

Figure 4.2. Illustration of the types of waves depending on the value of the effective refractive index. The insets show the electric field, E, propagating in the z-axis (propagation direction).

4.2 Grating Couplers

Figure 4.3 depicts the typical fibre-to-PIC coupling assisted by a grating coupler used in silicon photonics. A tilted optical fibre is put on top of grating to inject (collect) the light to (from) the PIC. The grating coupler is made of a wide corrugated waveguide that serves to redirect the light to/from the PIC. Because the grating is much wider than the typical silicon strip waveguide, an adiabatic taper is used to interface both without optical losses.

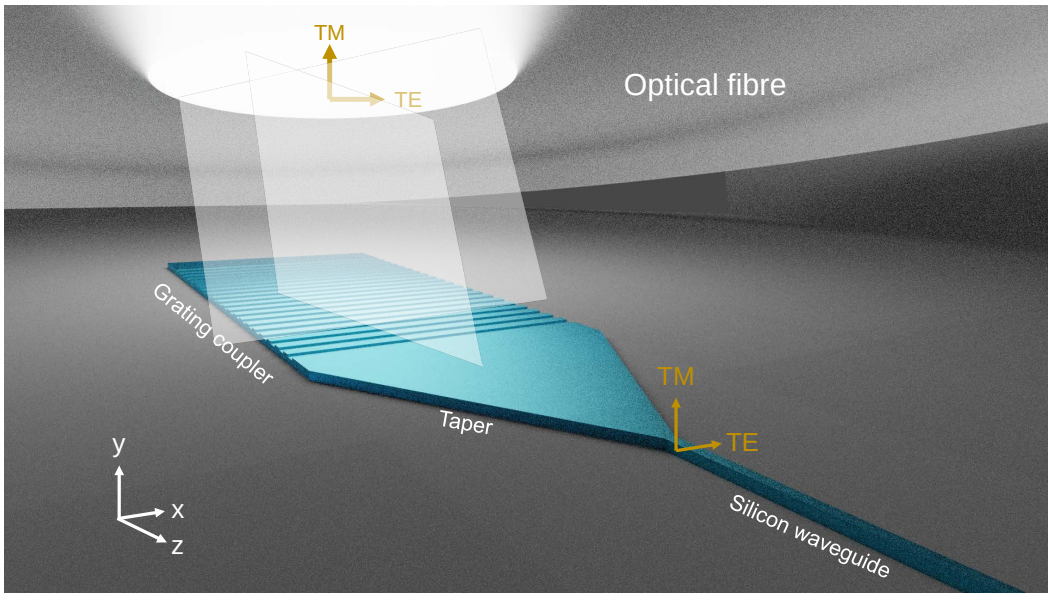

Figure 4.3. Illustration of a fibre-to-PIC coupling configuration using a grating coupler.

Grating couplers are a diffractive structure based on a wide waveguide with an engineered refractive index distribution along the propagation direction. Typically, the index profile is obtained by etching grooves on the wide silicon waveguide and this can be either periodic (uniform grating couplers) or non-periodic (chirped or apodized gratings) [20]. The cross-section of a uniform grating coupler is depicted in Fig. 4.4. At the bottom the silicon substrate acts as a partial reflector. The thickness of the buried oxide layer (BOX) of typical standard silicon on insulator wafers range between 1 and 3 µm and affects to the performance of the grating [21]. In this work is set to the typical value of 2 µm found in standard silicon-on-insulator wafers. On top of the silicon waveguide (Si-WG) a protecting oxide upper-cladding is deposited. The thickness of this layer depends on the devices that comprise the PIC. In this work is set to 1 µm. The silicon waveguide has different grooves which we call unit cells. These cells have a length, Λ, or a pitch in the case of being a uniform grating. Each cell is comprised of an etch and non-etch region. The depth of the etch, t_{etch}, is typically set to 70 nm in SOI gratings in order to obtain the best performance. Finally, the relation between Λ and the length of the etch region is called the fill- or filling-factor, f.

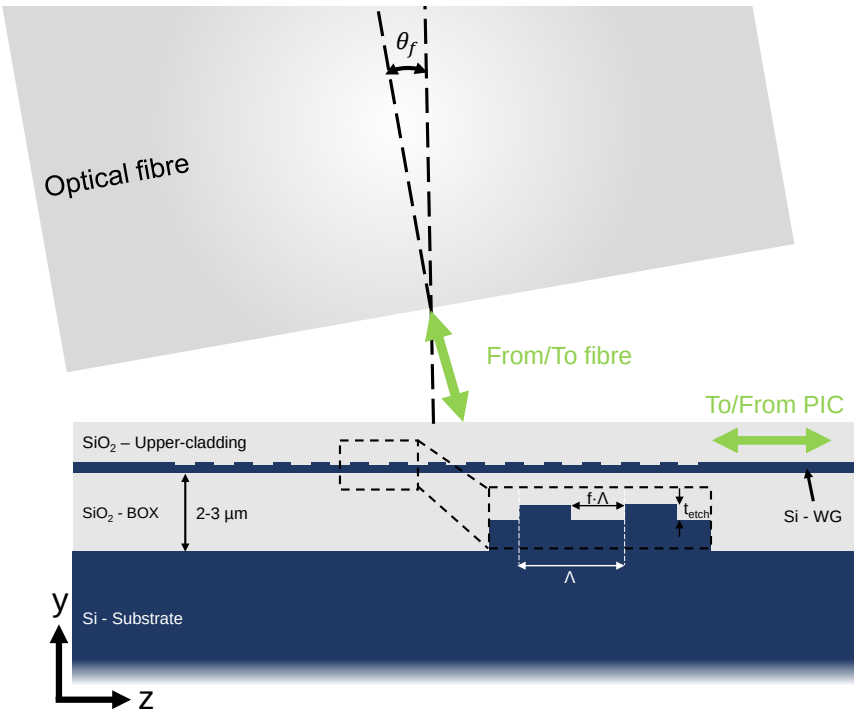

Figure 4.4. Cross-section of a uniform grating coupler. The zoom-in shows the detail of the grating grooves.

On the other hand, because the grating is much wider ($\sim$ 12 µm) than higher ($<$ 0.5 µm) and invariant in the y-axis, this can be approximated as a slab waveguide in the x-z plane[1] (see. Fig. 4.4). This approximation facilities and can speed up up to three orders of magnitude the simulation of the structure.

[1] If the grating is not invariant as it is the cased of focusing grating couplers [22], this approximation is not valid and the whole structure should be simulated.

4.2.1 Working Principle

The working principle of grating couplers rely on the Bragg condition and by considering only the first diffracted mode [23]. From this, the well-known phase-matching equation is established:

$$\Lambda = \frac{\lambda}{n_{eff} - n_c \sin\theta} \tag{4.6}$$

where Λ is the pitch or the length of a unit cell, λ is the working wavelength, n_{eff} is the effective refractive index that experiences the light through the unit cell, n_c is the cladding refractive index and θ is the angle of incidence of the light into/from the grating. Due to the SiO_2 upper-cladding, this angle does not correspond to the physical tilt of the fibre, θ_f, which is typically 10^o. Hence, by using the Snell's law Eq. (4.6) is rewritten as:

$$\Lambda = \frac{\lambda}{n_{eff} - \sin\theta_f} \tag{4.7}$$

The value of n_{eff} can be usually obtained as the average, n_{avg}, between the effective refractive index in the etched, n_{etch}, and non-etched region, n_{wg}, [Eq. (4.8)]. However, it has to be highlighted that this expression is valid if the difference between n_{etch} and n_{wg} is small. Otherwise, numerical simulations should be carried out to obtain an accurate value.

$$n_{avg} = f n_{etch} + (1 - f) n_{wg} \tag{4.8}$$

4.2.2 Performance Parameters

Although the phase-matching equation serves to obtain the physical parameters of the grating, this does not tell us a about the resulting performance. The performance of grating coupler is assed by the following parameters and are obtained simulating the structure with rigorous numerical simulation methods such as finite-difference time-domain (FDTD):

- **Directionality**: The amount of diffracted power from the grating to the optical fibre at a given wavelength.
- **Coupling efficiency (CE)**: The overlap between the fibre optical mode and the power arriving to the fibre at a given wavelength. This is mathematically defined by the overlap integral [23]:

$$\eta = \left| \int\int \boldsymbol{E} \times \boldsymbol{H_{fib}}^* dS \right|^2 \tag{4.9}$$

  where $\boldsymbol{E}$ is the E-field of the diffracted wave from the grating, $\boldsymbol{H_{fib}}^*$ is the complex conjugate of the H-field of the fibre mode and S is the fibre facet.
- **Back-reflections**: The amount of reflected power that occurs due to the impedance mismatch between the grating index profile and the silicon slab waveguide.
- **CE bandwidth**: The range of wavelength in which the coupling efficiency is higher than a certain value, usually 1 dB, in respect to the maximum or a given wavelength.

- **Polarization-dependence loss (PDL)**: The difference of coupling efficiency in dB between both polarizations.

- **PDL bandwidth**: The range of wavelength in which the PDL is lower than a certain value in respect to the minimum ir a given wavelength.

4.2.3 Polarization Dependency

The phase-matching equation [Eq. (4.6)] and thus, the grating coupler, is polarization dependent because the n_{eff} term. Indeed, standard grating couplers acts as a polarizing filter. This is shown in Figs. 4.5a and 4.5b where it is represented the coupling efficiency as a function of the wavelength of both polarizations for standard TE (Fig. 4.5a) and TM (Fig. 4.5b) optimized grating couplers. Both structures present PDL greater than 20 dB in the telecom C-band (1530-1565 nm) which are too high for the current PIC requirements.

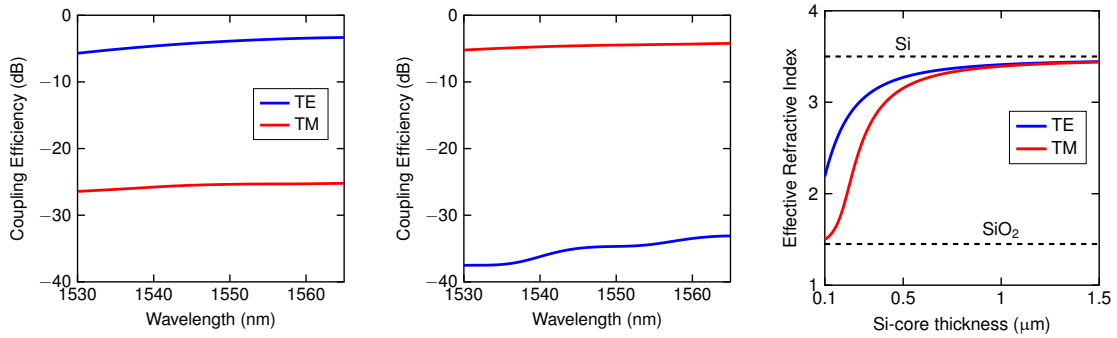

Figure 4.5. Coupling efficiency spectra for TE and TM polarization of: **(a)** TE and **(b)** TM optimized grating couplers. Both gratings have 20 periods, 70 nm of etch and are designed for $\lambda = 1550$ nm. The silicon waveguide is 220-nm-thick. **(c)** Fundamental mode effective refractive index of a SiO_2/Si waveguide for TE and TM polarization as a function of the Si-core thickness. Results are given at $\lambda = 1550$ nm.

In a SiO_2/Si slab waveguide the effective refractive index of the fundamental mode for TE polarization is always greater than TM for thickness below 1 μm (see Fig. 4.5c). Using greater thicknesses could be a solution by depositing a layer of amorphous silicon on top of the grating waveguide by plasma-enhanced chemical-vapour deposition (PECVD) [24, 25]. However, due to the large thickness mismatch between the grating waveguide and the strip silicon waveguide the coupling between them suffers from high optical losses. Furthermore, because the grating waveguide would be highly multimode this presents high-order Bloch modes which complicate the grating design [26]. Therefore, taking into account that in standard SOI wafers the silicon thickness ranges between 220 nm and 400 nm, other approaches for achieving polarization-independence should be explored. As stated in section 1.2, using subwavelength structures could enable this condition together with a high-performance response.

4.3 Subwavelength Integrated Photonics

Subwavelength integrated photonics is the field of periodic photonic structures with a sufficiently low pitch, Λ_{SWG}, that suppress diffraction effects. In this work, we deal with subwavelength structures made of isotropic materials such are SiO_2 and Si. By using this kind of structures, the optical properties can be engineered which results in an increase of the performance of the typical building-blocks used in PICs [27, 28].

Depending on how the light impinges into the subwavelength structures (see Fig. 4.6), these can be classified in two types: (i) lengthwise and (ii) crosswise. In the first case, the light travels through the periodicity direction –which is in the x-axis–, whereas in the second case, the light travels normally to the periodic direction, i.e., in the z-axis. In this work, we deal with crosswise subwavelength periodic structures since they exhibit a strong birefringence which can be exploited for designing polarization-insensitive grating couplers.

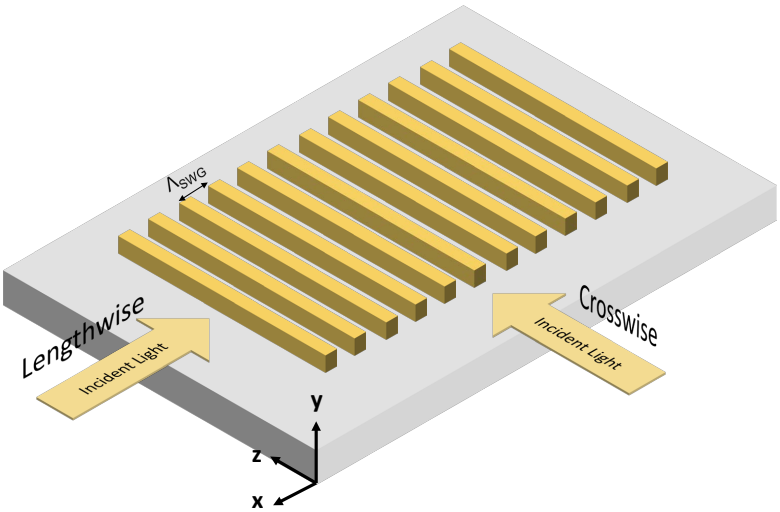

Figure 4.6. Illustration of a subwavelength periodic structure made of two different materials. The periodicity is along the x-axis. If the light impinges from the z- or y-axis the structure is referred as crosswise. Conversely, if the light comes form the x-axis, this is referred as lengthwise.

4.3.1 Crosswise Subwavelength Periodic Structures as Uniaxial Dielectric Metamaterials

Let us imagine periodic structure form by a stack of two materials with permittivity ε_A and ε_B, where light impinges normally to the periodicity. This is depicted in Fig. 4.7a, where a plane wave impinges normally into a stack of material of thickness a and b with permittivities ε_A and ε_B, respectively. The stack is periodic along the x-axis with a pitch $\Lambda_{SWG} = a + b$ and extends infinitely in both y- and z-axis. If the relation between the pitch and the wavelength of the incident wave is small enough, then the periodic structures acts as a UHL material with and effective permittivity, ε_{eff}. The equivalent metamaterial behaves as a uniaxial crystal with different permittivities

depending whether the light is TM-polarized, $\varepsilon_{||}$, (Fig. 4.7b) or TE-polarized, $\varepsilon_{\perp}$, (Fig. 4.7c).

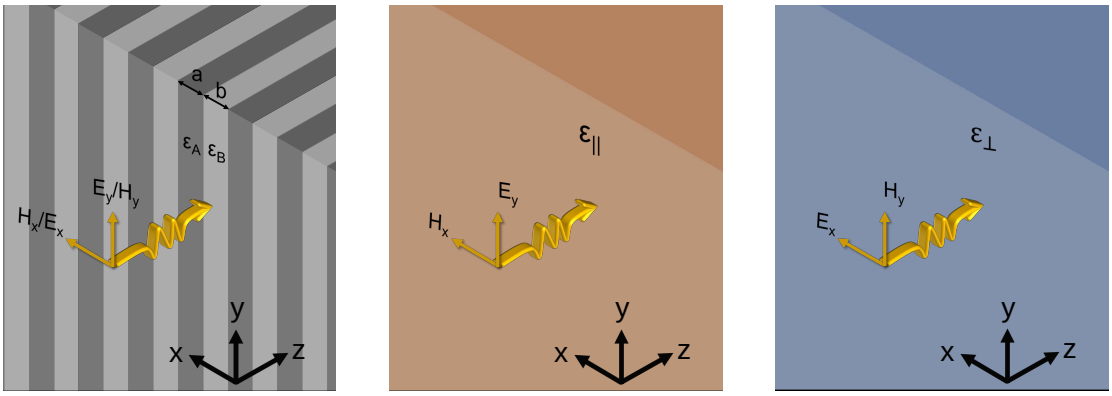

(a) **(b)** **(c)**

Figure 4.7. **(a)** Illustration of a plane wave with TE (E_x,H_y) or TM (E_y,H_y) polarization impinges along the z-axis from an isotropic homogenous medium to a subwavelength one formed by a periodic stack of homogeneous materials with ε_A and ε_B permittivities. **(b,c)** Equivalent permittivity of the subwavelength medium when the incident wave is **(b)** TM and **(c)** TE polarized.

The value of $\varepsilon_{\perp}$ and $\varepsilon_{||}$ can be obtained by using FEM or solving the dispersion-relation equation which is obtained after some cumbersome steps by applying the transfer matrix method (TMM) and the Floquet theorem to a two-layer periodic structure [29–31] (see Appendix B):

$$\cos(k_x \Lambda_{SWG}) = \cos(k_{z,a} a)\cos(k_{z,b} b) - \Delta \sin(k_{z,a} a)\sin(k_{z,b} b) \tag{4.10}$$

where

$$k_{z,a/b} = \frac{2\pi}{\lambda}\sqrt{\varepsilon_{a/b} - \varepsilon_{eff}} \tag{4.11}$$

and Δ depends on the light polarization:

$$\Delta^{TE} = \frac{1}{2}\left(\frac{\varepsilon_b k_{z,a}}{\varepsilon_a k_{z,b}} + \frac{\varepsilon_a k_{z,b}}{\varepsilon_b k_{z,a}}\right) \tag{4.12}$$

$$\Delta^{TM} = \frac{1}{2}\left(\frac{k_{z,a}}{k_{z,b}} + \frac{k_{z,b}}{k_{z,a}}\right) \tag{4.13}$$

Since the light propagates only in the z-axis, the term k_x equals zero. Therefore, the Eq. (4.10) has no analytical solution and numeric root finding methods are necessary. However, if the relation between the pitch and the wavelength is small enough, the Eq. (4.10) can be accurately approximated to the zero-order of a Taylor expansion by using the effective medium theory (EMT)[2]. The approximation for both polarizations is the well-known Rytov's formulas [35] and are given by Eqs. 4.14 and 4.15 for TM and TE polarization, respectively. If the relation is not small enough, a second order

[2]The effect medium theory is a well-known theory to calculate the equivalent optical properties of heterogeneous materials. Among the different methods, the Maxwell-Garnett is the most popular [32–34].

approximation can be used [36]. However, in this case it is preferred to obtain the exact solution by solving Eq. 4.10.

$$\varepsilon_{||} = \frac{a}{\Lambda_{SWG}}\varepsilon_A + \frac{b}{\Lambda_{SWG}}\varepsilon_B \tag{4.14}$$

$$\frac{1}{\varepsilon_{\perp}} = \frac{a}{\Lambda_{SWG}}\frac{1}{\varepsilon_A} + \frac{b}{\Lambda_{SWG}}\frac{1}{\varepsilon_B} \tag{4.15}$$

4.3.2 The Deep-Subwavelength Regime: Influence of the Pitch and Wavelength Relation

In the previous subsection we have stated that a periodic subwavelength structure behaves as a UHL dielectric metamaterial if the relation between the pitch and the wavelength is small enough. However, the term "small enough" has not been rigorously defined. By using the Bragg's condition, it can be proved that if the pitch fulfils:

$$\Lambda_{SWG} < \frac{\lambda}{\max(\sqrt{\varepsilon_A}, \sqrt{\varepsilon_B})} \tag{4.16}$$

then diffraction is not allowed and the light travels through the subwavelength structure with a phase given by the dispersion-relation expression [Eq. (4.10)]. However, this does not mean that the subwavelength structure behaves as a homogeneous material. If $\Lambda/\lambda \to 0$ is not accomplished, leaky modes could arise at the interface which can tunnel through the structure if it is not long enough [37]. Therefore, the material cannot be treated as homogenous. On the other hand, under some special conditions, to fully model the metamaterial as homogenous this must present some magnetic response in order to match both impedance and phase properties [38].

Being able to accurately approximate the periodic structure as a UHL material is necessary to simulate the grating coupler cross-section instead of the whole structure due to computer resources constrains and in order to speed up the design procedure. However, setting the value of Λ_{SWG} for this thesis in which the periodic structure can be treated as a UHL material is not trivial. The analysis has to be done throughout the following aspects: (i) inspecting the dispersion-relation equation; (ii) analyse the field profile inside the periodic structure; and (iii) investigate the transmittance/reflectance values when it is interfaced with an homogenous material. For this work, the materials used for the investigated periodic stack are the same that comprise the grating coupler: Si ($\varepsilon_r = 12.08$) and SiO_2 ($\varepsilon_r = 2.085$) at $\lambda = 1550$ nm. Moreover, for the ease of calculations, the thickness of both layers is set to $a = b = \Lambda_{SWG}/2$.

Dispersion-relation

The dispersion-relation equation [Eq. (4.10)] is first investigated by obtaining the real solutions for both polarizations as a function of the pitch. As shown in Fig. 4.8a, for pitch values lower than $\lambda/n_{Si} = 445$ nm only the zero order is allowed, in accordance with Eq. (4.16) and the structure is in the subwavelength regime. It has to be noticed that the lower the pitch the higher the birefringence between the effective refractive index of both polarizations. As it is later explained in subsection 4.4.1, large birefringence values are beneficial for designing polarization-insensitive grating couplers. When the

subwavelength condition is lost, high-order modes begin to arise and ultimately, when $\Lambda_{SWG} \to +\infty$ the structure is seen as pure Si and all the solutions converge to the plane wave solution.

On the other hand, a comparison between the rigorous solution given by Eq. (4.10) and the Rytov's approximation (Eqs. (4.15) and (4.14)) is shown in Fig. 4.8b. As it can be noticed, the approximation is only accurate for pitch values lower than $\sim$ 100 nm and for higher values can only be used to estimate the values of the equivalent refractive index.

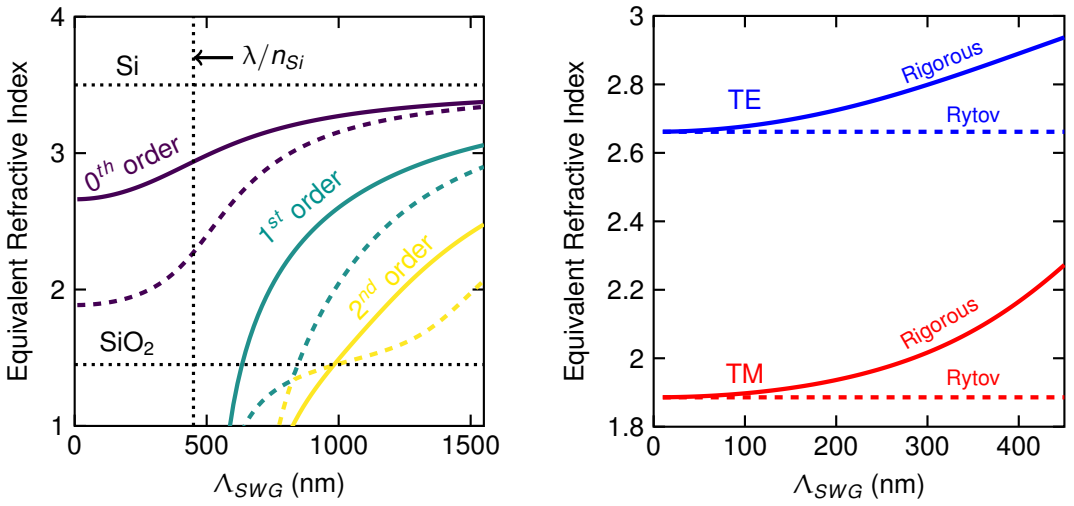

Figure 4.8. **(a)** Equivalent refractive index for TM (solid line) and TE (dashed line) polarized light as a function of the subwavelength pitch using Eq. (4.10). **(b)** Comparison between Rytov's approximation [Eqs. (4.14) and (4.15)]. Equivalent refractive index for both polarizations as a function of the subwavelength pitch. Results are show the different supported solutions at 1550 nm and for a Si/SiO_2 stack.

Regarding the imaginary solutions, corresponding to the leaky modes, we obtain differences between approximating the periodic stack as an equivalent homogenous material and solving Eq. (4.10). In a homogenous medium the imaginary solutions of n_{eff} are antisymmetric, i.e., $n_{eff}(m) = -n_{eff}(-m)$ where m is the m^{th} imaginary solution (see Appendix C.1). However, in a periodic subwavelength medium –aside from being the calculus of the values much more complex– the solutions given by Eq. (4.10) are not antisymmetric (see Appendix C.2) and only approximates to be when the pitch is $\sim$ 100 nm or lower.

Field profile

Then, the field profile of the zero-order mode is investigated. Recalling Maxwell's equations, a plane wave travelling through a homogenous medium has only one component in both E- and H-fields with a constant value in the axis transverse (x-axis) to the propagation direction (z-axis). However, in a crosswise subwavelength periodic medium two components (transverse and longitudinal) in the E- or H-field (depending on the polarization) exists being not constant in the x-axis. The different profiles of the field

components are obtained by implementing the TMM with eigenmode expansion and mode-matching [30, 39] (see Appendix B) in MATLAB [40].

First, the transverse component of the field is investigated. For both polarization these are depicted in Figs. 4.9a and 4.9b, respectively, for different pitch values. It can be noticed how as the pitch is reduced the peak-to-peak value of the field diminishes being negligible for pitch values lower than 100 nm and approximates to a plane wave.

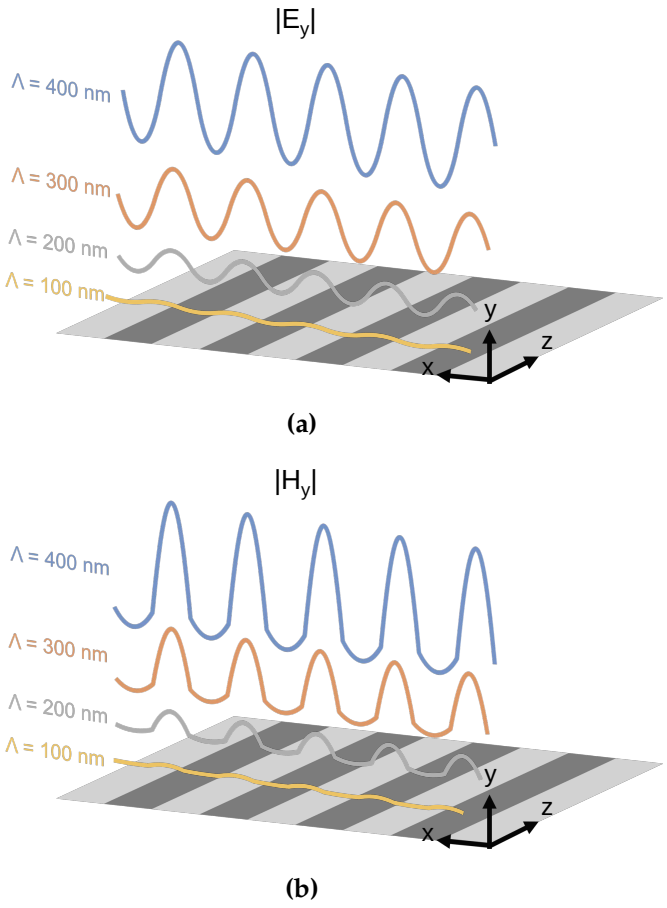

Figure 4.9. Field profiles obtained by TMM for different values of pitch. **(a)** TM and **(b)** TE polarization. Results are given for a Si/SiO_2 stack at $\lambda = 1550$ nm.

Secondly, in order to investigate the influence of the longitudinal component the ellipse of polarization is represented as a function of the pitch in Figs. 4.10a and 4.10b for TE (E_x and E_z) and TM (H_x and H_z) polarization, respectively. The ellipse is given at the interface of the Si/SiO_2 stack. The interface point is chosen since is the worst case because the longitudinal component attains its maximum value. As it can be noted, for both polarizations the polarization ellipse tends to close as the pitch is reduced, i.e., only exists the transverse component as in a homogenous medium. Furthermore, for TE this is more accused than TM because in this latter $E_z \propto \varepsilon(x)$. On the other hand, the axial ratio is obtained as $|\phi_x/\phi_z|$ and is depicted in Fig. 4.10c. For a plane wave in the axial ratio is infinity, however, in subwavelength medium this is not accomplished as noted.

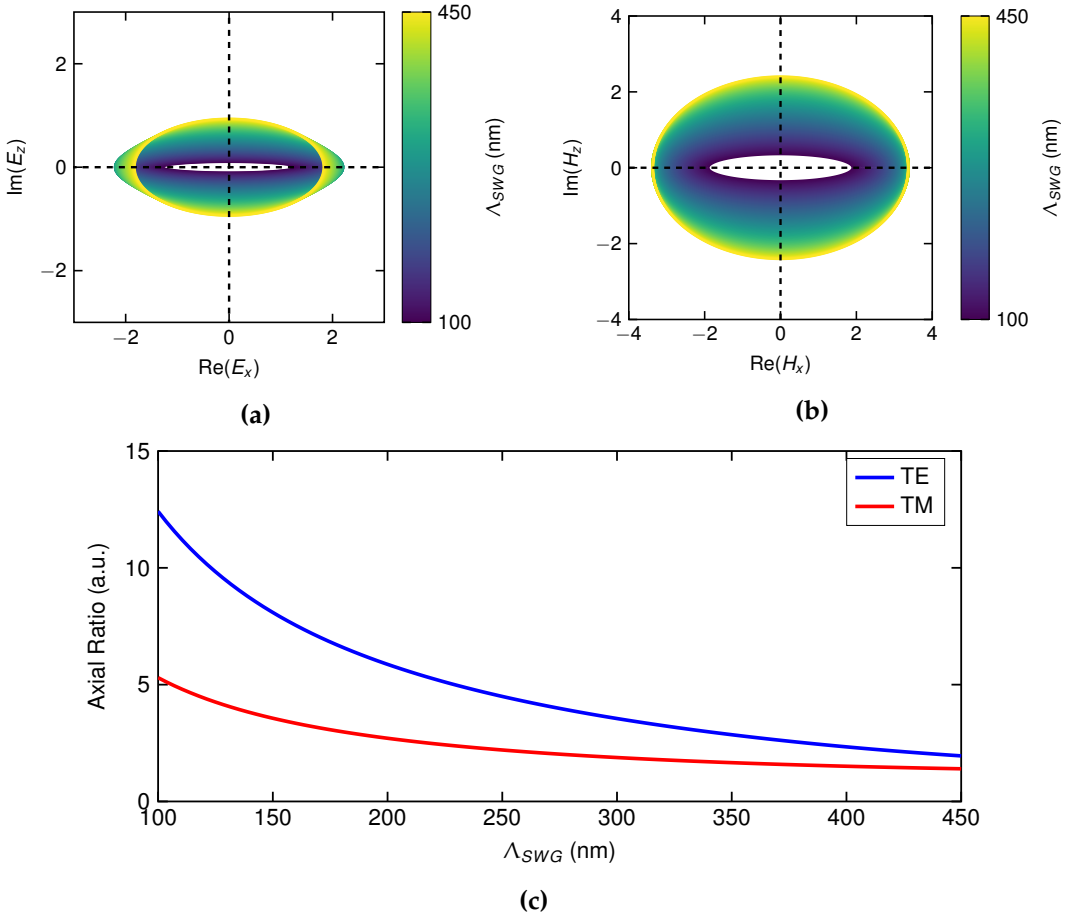

Figure 4.10. Ellipse of polarization for **(a)** TE and **(b)** TM polarization as a function of the pitch. **(c)** Axial ratio for both polarizations as a function of the pitch. Results are obtained for a Si/SiO_2 stack at $\lambda = 1550$ nm.

Interface with a homogenous material

The existence of a non-constant field along the x-axis has to be taken into account when the subwavelength structure is interfaced with a homogenous material. In order to fulfil boundary conditions, significant leaky modes may arise at the interface and thus, prohibit to approximate the periodic stack as a homogenous material.

To analyse this behaviour, we now consider the previous SiO_2/Si stack (medium II) interfaced with silicon (medium I). A plane wave travels in the z-axis from the medium I and impinges into the medium II. The field profile at the interface of Si and the Si/SiO_2 stack and each medium is obtained using methods of Appendix C.1-C.3. In contrast with other simulation methods such as FDTD, the utilization of eigenmode expansion allows to discriminate between the propagates modes ($m = 0$) and the leaky modes ($m \neq 0$) and thus, obtain an insight of the phenomena that occurs within the structure. Calculations are obtained for both polarizations and a pitch value of 400 nm and 100 nm. The first is in the limit of the subwavelength condition whereas the latter approximates to a homogenous material from previous results.

In Fig. 4.11 is depicted the field distribution (x,z) for $\Lambda_{SWG} = 400$ nm of the $|E_y|$

(Fig. 4.11a) and $|H_y|$ (Fig. 4.11b) components for the TM and TE polarized waves, respectively. As it can be noticed, leaky modes at the interface perturb the adjoint wave between the two media for both polarizations. However, for TE polarization, they extend further in the z-axis. Therefore, if several homogenous/subwavelength media are stacked along the z-axis with a pitch lower than 200 nm, then the leaky waves interact with the propagated wave due the cavity behaviour of the stack. Consequently, the subwavelength medium cannot be approximated to homogenous. However, if the subwavelength is decreased to 100 nm, leaky waves are negligible as shown in Fig. 4.12 and thus, the homogenous approximation may be accurate.

The homogenous approximation can be checked by obtaining the transmittance and reflectance parameters of the propagated mode ($m = 0$). From these, the relative permittivity and permeability that fulfil the impedance of an equivalent homogenous medium is calculated using methods of Appendix C.4.2 and compared with that obtained using the value from Eq. (4.10). Results are depicted in Fig. 4.13. For TM polarization, the impedance given by the dispersion-relation equation agrees with that obtained from the eigenmode expansion and mode-matching for pitches. The equivalent homogeneous material presents lossless dielectric behaviour (Fig. 4.13a) with non-magnetic response (Fig. 4.13b). However, for TE polarization, despite the lossless behaviour, the equivalent permittivity is greater than that obtained from Eq. (4.10) (Fig. 4.13c). Furthermore, the equivalent homogenous material presents a diamagnetic response for pitch values larges than 100 nm.

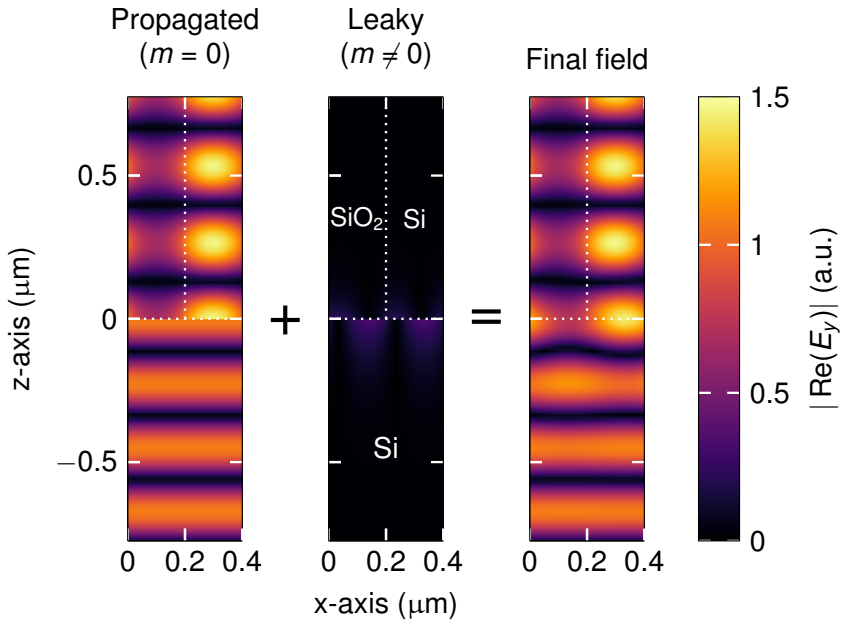

(a)

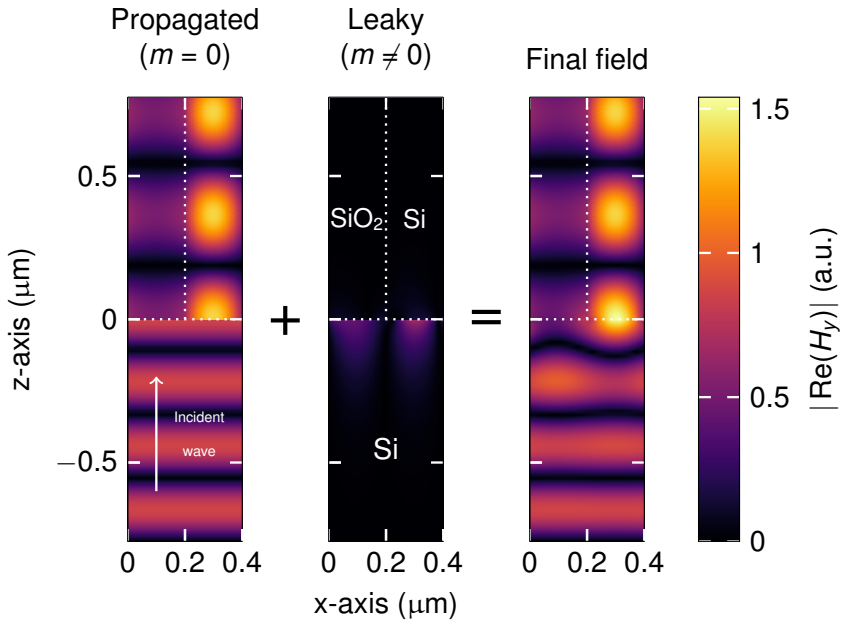

(b)

Figure 4.11. Field profiles (propagated + leaky) obtained by eigenmode expansion and mode-matching when a plane wave in a homogenous medium made of Si (medium I) impinges into a crosswise subwavelength structure made of a Si/SiO_2 stack with a 400 nm pitch (medium II). The final field is the superposition of the propagated mode with the leaky modes that arise at the interface between medium I and II. Results are given for **(a)** TE and **(b)** TM polarization at 1550 nm.

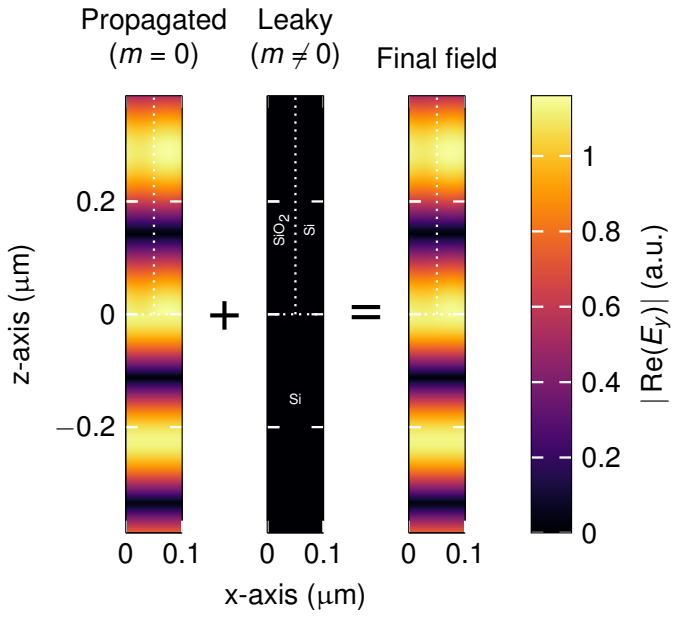

(a)

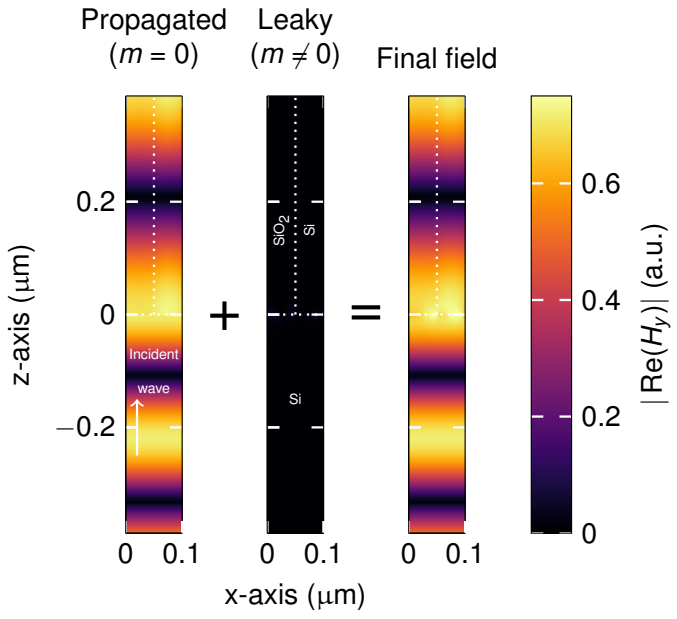

(b)

Figure 4.12. Field profiles (propagated + leaky) obtained by eigenmode expansion and mode-matching when a plane wave in a homogenous medium made of Si (medium I) impinges into a crosswise subwavelength structure made of a Si/SiO_2 stack with a 100 nm pitch (medium II). The final field is the superposition of the propagated mode with the leaky modes that arise at the interface between medium I and II. Results are given for **(a)** TE and **(b)** TM polarization at 1550 nm.

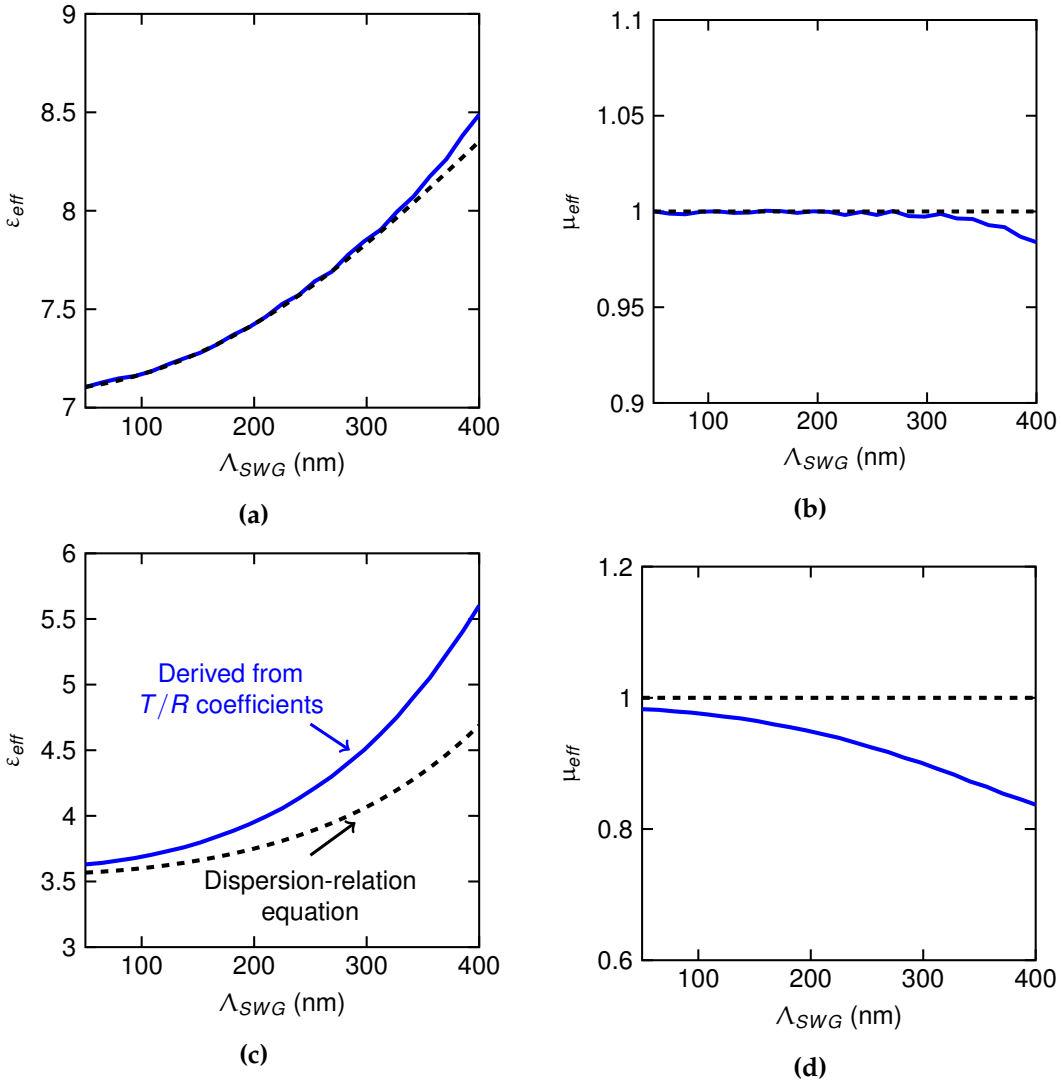

Figure 4.13. Effective **(a,c)** permittivities and **(b,d)** permeabilities as a function of the pitch for **(a,b)** TM and **(c,d)** TE polarization. The dotted line stands for the value given by Eq. (4.10). Results are obtained for a medium formed by a homogenous material (Si) and two-layer stack (SiO_2/Si) at $\lambda = 1550$ nm.

Fig. 4.14 summarizes the behaviour of a crosswise periodic structure used in this work as a function of the pitch for both polarizations. Although the crosswise periodic structure can be approximated to as a stand-alone homogenous material for pitches lower than $\sim$ 400 nm. The large evanescent field and the magnetic response of TE polarization are not convenient to use it for polarization-independent grating couplers were the leaky modes are expected to interact between the unit cells. Furthermore, introduce a magnetic response in this kind of structure implies to highly complicate simulations. Therefore, we choose 100 nm as the pitch for the crosswise subwavelength structure used for the design of the polarization-independent grating couplers.

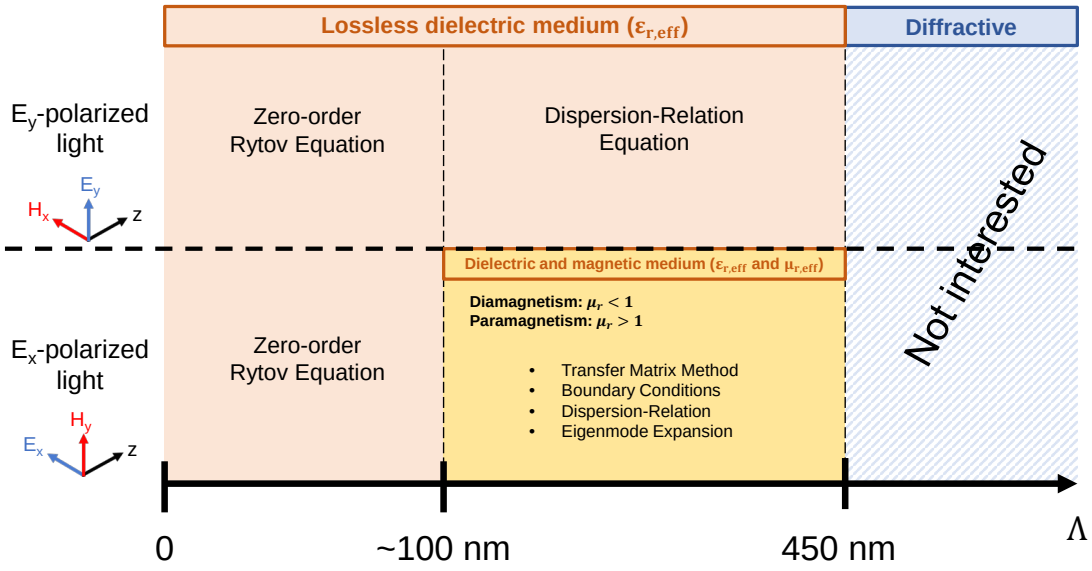

Figure 4.14. Behaviour and methods used to describe the optical properties as a function of the pitch of the subwavelength structure used in this work.

4.3.3 Tuning the Equivalent Refractive Index

There are two approaches for tuning the equivalent refractive index for a given pitch. The first one is by changing the fill factor (see Fig. 4.15a), i.e., $f_{SWG} = a/\Lambda_{SWG}$ as it can derived from Rytov's equations [Eqs. (4.15) and (4.14)]. The second one is based on titling the periodic structure (see Fig. 4.15b) in order to change the amount of birefringence [41]. The titling approach needs of further investigation in order to validate for both polarizations the resulting non-diagonal tensor of the equivalent permittivity. Hence, in this thesis, the fill-factor approach we will be used for tuning the optical properties.

Figure 4.16a shows the equivalent refractive index as a function of the filling factor using the zero-order approximation given by Rytov. As it can be noticed, TM polarization exhibits larger refractive index than TE which will enable the polarization-independence condition in grating couplers as it is explained afterwards. Furthermore, the birefringence (Δn) can be as large as 0.8 for filling-factors of around 40% and greater than 0.2 for almost the whole range (see Fig. 4.16b).

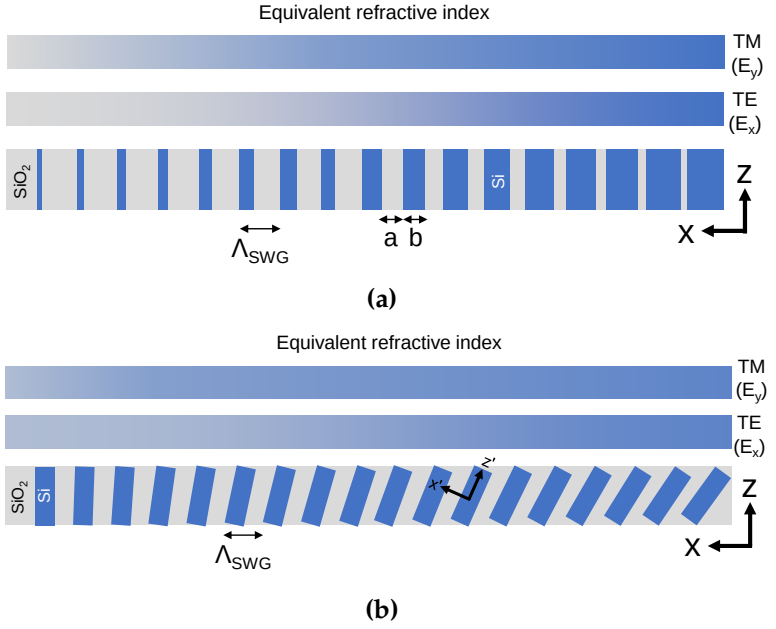

Figure 4.15. Different ways of tuning the equivalent refractive index of a crosswise periodic subwavelength structure. **(a)** Changing the fill-factor that occupies each layer and **(b)** tilting the layers.

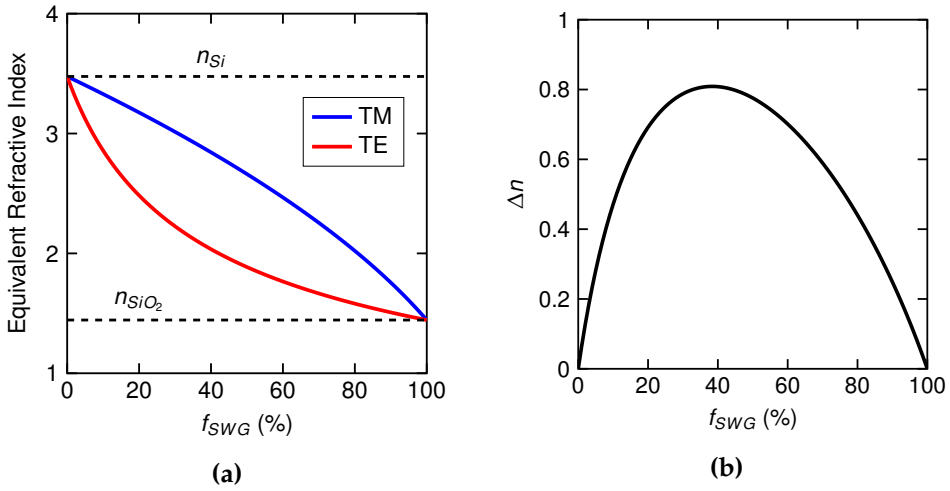

Figure 4.16. **(a)** Equivalent refractive index and **(b)** associated birefringence, Δn, as a function of the fill-factor of the periodic structure. Results are given for a stack of SiO_2/Si using Rytov's expressions [Eqs. (4.15) and (4.14)].

4.4 Polarization-Independent Grating Couplers Enabled by Dielectric Metamaterials

In the previous subsection it has been shown how and in which conditions crosswise periodic structures can be act and used as uniaxial dielectric homogenous metamaterials. The aim of this subsection is to exploit its birefringence for enabling polarization-independent grating couplers. To this end, the etched regions, known as trenches, of a typical shallowed-etched grating (see Fig. 4.17a) are replaced by a periodic subwavelength structure (see Fig. 4.17b). This is made by full-etching the silicon waveguide and the equivalent refractive index is tuned by changing the subwavelength fill-factor. Therefore, from the polarization point of view, two different gratings are seen for TE an TM polarization because of the birefringence of the subwavelength structures.

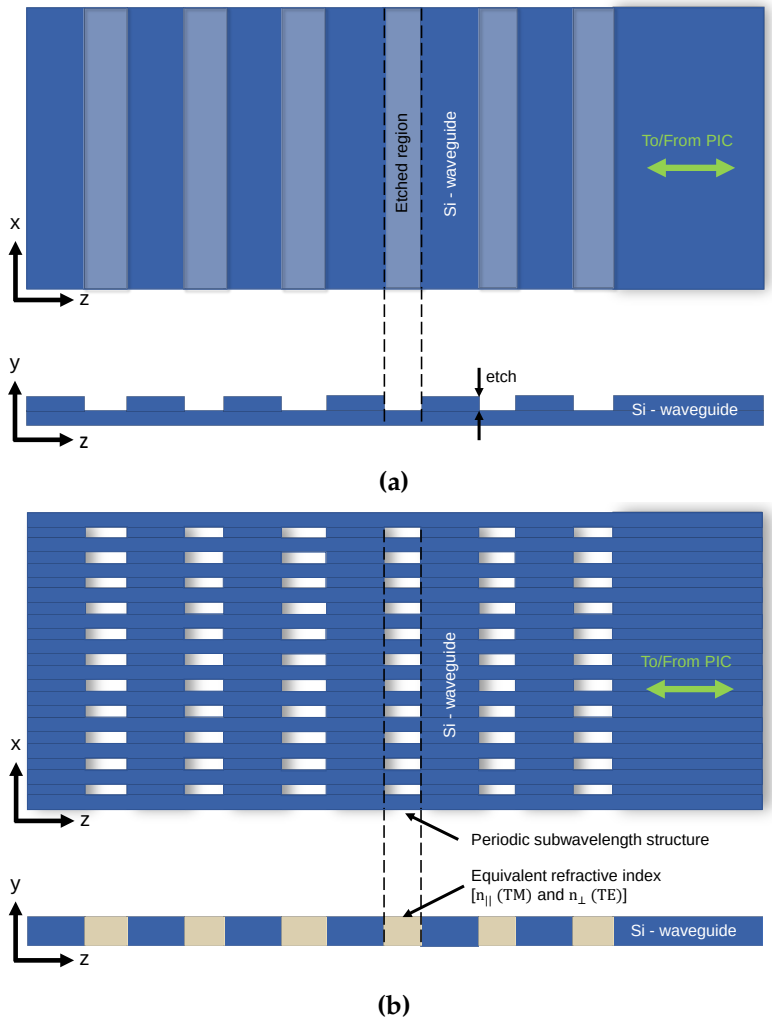

Figure 4.17. Top-view and cross-section of grating couplers made by: **(a)** Shallow etching and **(b)** full etching the grating including a subwavelength structure. These latter act as an equivalent refractive index as a function of their pitch and fill-factor.

4.4.1 Influence of the Waveguide Thickness: Beyond the Standard Thickness

To allow the polarization-independence condition in the grating phase-matching equation [Eq. (4.6)] the value of n_{eff} must be the same for both polarizations. By using the approximation of n_{avg} [Eq. (4.8)] and after some manipulations, the resulting fill-factor that matches both n_{avg} for TE and TM is:

$$f = \frac{n_{wg}^{TE} - n_{wg}^{TM}}{(n_{etch}^{TM} - n_{etch}^{TE}) + (n_{wg}^{TE} - n_{wg}^{TM})} = \frac{1}{1 + \dfrac{n_{etch}^{TM} - n_{etch}^{TE}}{n_{wg}^{TE} - n_{wg}^{TM}}} = \frac{1}{1 + \dfrac{\Delta n_{etch}}{\Delta n_{wg}}} \tag{4.17}$$

and being the condition of Eq. (4.18) required since the value of f should be comprised between 0 and 1 and Δn_{wg} is always positive.

$$(n_{etch}^{TM} - n_{etch}^{TE}) > 0. \tag{4.18}$$

In a typical polarization-dependent grating coupler, this condition cannot be fulfilled since the refractive index of TE is always greater than TM regardless of the waveguide thickness and thus, $(n_{etch}^{TM} - n_{etch}^{TE}) < 0$, which leads to values of f greater than 1. However, if the etched waveguide is replaced by a crosswise subwavelength structure, then is possible to obtain $(n_{etch}^{TM} - n_{etch}^{TE}) > 0$ and thus, exists a value for f between 0 and 1.

For this new case, the thickness of the grating waveguide plays an important role. The thicker the waveguide the larger the interval of the fill-factor in the unit cell of the grating. The best case or the lower-limit of the fill-factor is given when Δn_{etch} attains its maximum value, i.e., when subwavelength structure achieves the maximum birefringence ($f_{SWG} = 0.4$). For this latter, the value of Δn_{wg} and Δn_{etch} is depicted as a function of the waveguide thickness in Fig. 4.18a. As the thickness increases from the standard 220 nm, the difference between both increments decreases until they cross at around 320 nm. The associated minimum value of f is shown in Fig.4.18b. For a 220 nm thick waveguide, f ranges between 0.95 and 1, which is far from being optimal to achieve high grating performance. Thicker silicon layer which are non-standard but enlarge the fill-factor range may be more suitable for achieving better performance. Furthermore, in the context of developing polarization-independent PICs, the 320 nm has been proposed [42] which gives a lower-limit to the fill-factor of 0.5. Therefore, 320 nm is chosen as the thickness for the silicon layer of the gratings. On the other hand, regarding the upper-limit of the fill-factor, this is achieved when $n_{etch}^{TM} - n_{etch}^{TE} = 0$. For a 320-nm-thick waveguide this results for f_{SWG} value between 7% and 99.6% (see Fig. 4.16). Finally, minimum feature sizes below 10 nm can be obtained by electron beam lithography (EBL) [43, 44], hence, the upper- and lower-bounds of the subwavelength fill-factor are set to 0.1 and 0.9, respectively.

On the other hand, as stated in subsection 4.2.1, the value of n_{eff} can only be estimated as an average if the difference between the n_{etch} and n_{wg} is small (< 0.1). By replacing the trenches with subwavelength structures this condition does not fulfil. Hence, a adjusting or correction factor, Γ, should be introduced into the phase-matching equation, leading to:

$$\Lambda = \Gamma \frac{\lambda}{n_{avg} - n_c \sin\theta} \tag{4.19}$$

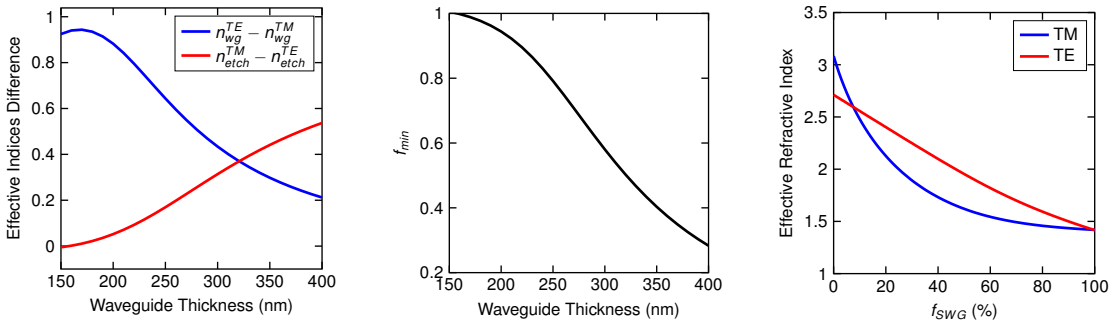

(a) **(b)** **(c)**

Figure 4.18. (a) Effective indices difference and **(b)** minimum attainable value of filling-factor, f_{min}, as a function of the waveguide thickness. Results are given for a stack of SiO_2/Si of $\Lambda = 100$ nm and $f_{SWG} = 40\%$ at $\lambda = 1550$ nm. **(c)** Effective refractive index as a function of the f_{SWG} value for a 320-nm-thick slab waveguide with the core made of the equivalent material of the aforementioned subwavelength structure.

Consequently, the Eq. (4.17) should rewritten as:

$$f = \frac{B(A-1) + (n_{etch}^{TE} - An_{etch}^{TM})}{(n_{etch}^{TE} - An_{etch}^{TM}) - (n_{wg}^{TE} - An_{wg}^{TM})} \tag{4.20}$$

where $A = \Gamma^{TE}/\Gamma^{TM}$, $B = n_c \sin\theta$ and value of Γ may range between 0.95 and 1.05 depending on the index difference between n_{etch} and n_{wg}.

4.4.2 The Diffraction Strength: An Optimization Problem

Before continuing, let us summarize the main parameters set at this point of the thesis for the grating coupler:

- Fibre tilt $\theta_f = 10^o$.
- Working wavelength $\lambda = 1550$ nm.
- Buried oxide thickness = 2 µm.
- Silicon waveguide thickness = 320 nm.
- SiO_2 upper-cladding thickness = 1 µm.
- The shallow etched waveguide regions are replaced by Si/SiO_2 full-etched crosswise subwavelength structures with:
  - Pitch $\Lambda_{SWG} = 100$ nm.
  - Fill-factor, f_{SWG}, between 10% (10 nm) and 90% (90 nm).
- Use of the correction factor Γ in the phase-matching equation.

The phase-matching equation is thus fulfilled for both polarizations for many possible f_{SWG} values. However, not all the solutions present the same performance. Indeed, the diffraction strength, i.e., the amount of power that is diffracted due to the impedance mismatch different waveguides, is different for both polarizations. In Fig. 4.19a is shown the coupling losses between a 320-nm-thick Si-slab waveguide and a metamaterial-slab waveguide comprised by the subwavelength structure as a function of the f_{SWG} value (see Appendix A.2 for methods). Coupling losses are greater for TM polarization because presents higher impedance mismatch compared to TE. The difference on the diffraction strength is increased with the fill-factor achieving its maximum for $f_{SWG} \approx 85\%$ as shown in Fig. 4.19b.

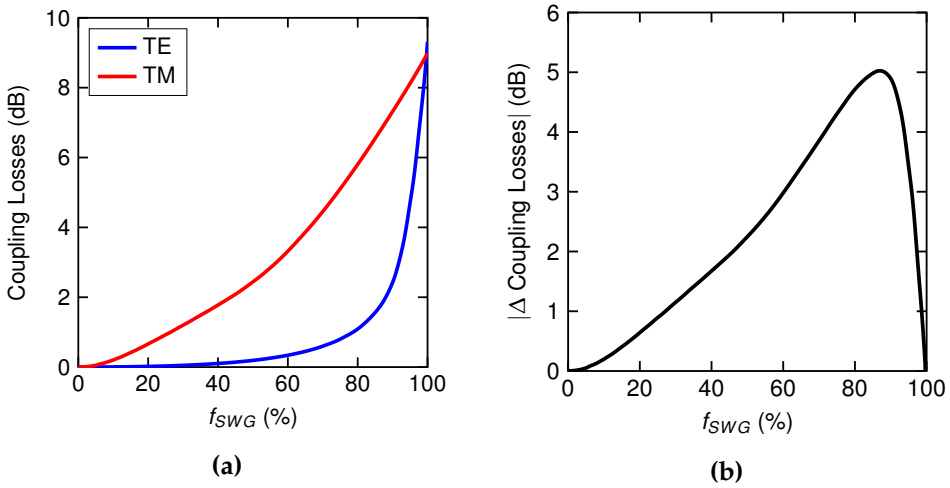

Figure 4.19. (a) Coupling losses and **(b)** increment between a 320-nm-thick Si and metamaterial waveguide as a function of the subwavelength filling-factor for both polarizations. Results are for a stack of SiO_2/Si of $\Lambda_{SWG} = 100$ nm at $\lambda = 1550$ nm.

Usually, the optimization of the grating would be made by carrying out a parametric scan of the variables. However, the large number of variables and possible solutions because of using subwavelength structures impossibilities to address this strategy. Furthermore, grating couplers need to be simulated by FDTD. Although FDTD is rigorous and can tackle any kind of electromagnetic structure, simulations are very long and the demand of computational resources is very high which translates to a low efficient method. Therefore, in order to address the optimization of polarization-independent grating couplers other approaches should be investigated.

4.5 Nature-Inspired Algorithms for Enabling High-Performance

Nature-inspired algorithms try to mimic the behaviour of nature to solve high-freedom degree problems. Among all algorithms, genetic algorithm (GA) and particle swarm optimization (PSO) stand out as the most famous for optimization all-kind of problems [45] and nanophotonic structures [46–48].

4.5.1 Particle Swarm Optimization

Particle swarm optimization is a nature-inspired algorithm that tries to mimic the behaviour of swarms such as birds or bees. The power of PSO applied to grating couplers has been demonstrated [49–55]. Hence, it is an ideal candidate to optimize our polarization-independent grating coupler.

The flow-chart of the algorithm is depicted in Fig. 4.20. The algorithm begins initializing the particles that comprise the swarm. The swarm is comprised of N particles, being each particle M-dimensional. In our case the particle refers to a grating, in which the variables are f_{SWG}, Γ^{TE} and Γ^{TM}. Therefore, by setting the number of unit cells to 20, each particle will be 60-dimensional. Then, the following steps are repeated N-times. First, the performance of the particles is evaluated with the fitness which assigns a cost to each particle. For each particle, if its cost is better (lower) than the previous iteration, then the pBest (particle best) is updated. Furthermore, among the particles, their positions is compared to the gBest (global best) which saves the best particle of all iterations. When the pBests and gBest are updated, if required, the velocity of each particle is updated to obtain the new position.

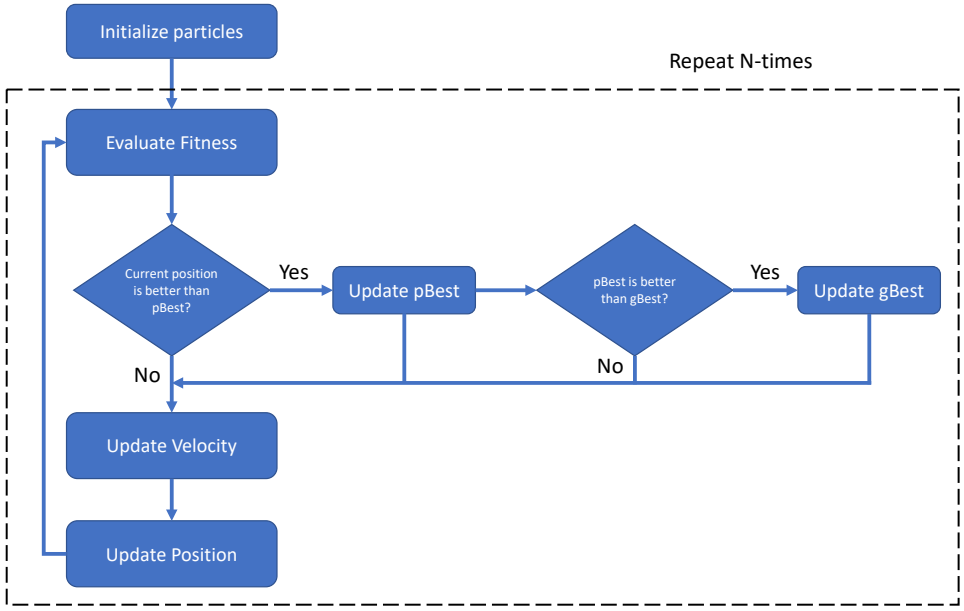

Figure 4.20. Flow-chart of the PSO algorithm.

The fitness of the particles, i.e., the performance of the grating is assed by using 2D-FDTD simulations for TE and TM polarizations (see Appendix A.3).

The velocity of the particles is calculated by using the following expression:

$$v_{nm}[i+1] = \omega v_{nm}[i] + c_1 r_{1,nm}[i](gBest_m[i] - x_{nm}[i]) + c_2 r_{2,nm}[i](pBest_{nm}[i] - x_{nm}[i]) \tag{4.21}$$

where ω is the inertia weight which prevent the particle from drastically change its direction, c_1 is the cognitive coefficient that is related to the memory of the previous best position, c_2 is the social coefficient and relates the neighbours, $r_{nm}[i]$ is a random number between 0 and 1 following a uniform distribution and $x_{nm}[i]$ stands for the

current position. The coefficients c_1 and c_2 impose a trade-off between exploration and exploitation, i.e., the ability to explore regions of the search space or to concentrate the search around a promising area, respectively. For instance, if $c_1 = c_2 > 0$ particles are attracted towards the average of the personal best position and the global best position. On the other hand, $c_2 > c_1$ is more beneficial for unimodal problems whereas $c_2 < c_1$ is better for multimodal problems.

Finally, the position is updated as:

$$x_{nm}[i+1] = x_{nm}[i] + v_{nm}[i+1] \tag{4.22}$$

Every nature-inspired algorithm is not exempt of possible issues. Most common are that the particles position do not convergence throughout iterations, the final solution is a minimum local or particle position go out of boundaries. Several solutions have been proposed to tackle these problems [56]. Among them, in this work we use the following strategies:

- Usually, the positions of particles are initialized to uniformly cover the search space. An efficient initialization method for the particle position is:

$$x_{nm}[0] = x_{\min} + r(x_{\max} - x_{\min}) \tag{4.23}$$

- To control the global exploration of particles, velocities are clamped to stay within the boundary constraints. The velocity clamping is defined as:

$$v_{nm}[i+1] = \begin{cases} v_{nm}[i+1] & if \quad v_{nm}[i+1] < v_{\max} \\ v_{\max} & if \quad v_{nm}[i+1] \geq v_{\max} \end{cases} \tag{4.24}$$

  where $v_{\max} = k(v_{ub} - v_{lb})$, being k a constant comprised between 0 and 1 and v_{up} and v_{lb} the upper- and lower-boundaries of the velocity. Moreover, if the particle is about to go further the boundary limits the velocity is set randomly in order to set the next position of the particle between boundaries.

- The inertia weight value is problem dependent. A common strategy is to start with a large values to facilitate the exploration and linearly decrease its value to promote exploration. Hence:

$$\omega[i] = (\omega[0] - \omega[N-1]) \frac{N-i}{N} + \omega[N-1] \tag{4.25}$$

  where $\omega[0] = 0.9$ and $\omega[N-1] = 0.4$.

- It has been shown that PSO has the ability to find optimum solutions with a small sizes of 10 to 30. In this work we will use 25 particles.

- Particles draw their strength from their cooperative nature, and are more effective when nostalgia (c_1) and envy (c_2) coexist in a good balance ($c_1 \approx c_2$).

4.5.2 The Figure of Merit

The fitness of the solutions is assessed by defining a figure of merit (FOM) that include the performance parameters shown in subsection 4.2.2. The FOM gives a value that should be minimized. Defining the right FOM is crucial to obtain the best solution and being its definition dependent on the required specifications. One must keep in mind that trade-off exist among the key performance parameters and at some optimization point, the optimizer will arrive the Pareto front in which one or some parameter will not be improved without diminishing other(s) [57].

In a grating coupler low optical losses and large bandwidth are desired, however, a trade-off exists between them (2D Pareto's front). Furthermore, in a polarization-independent grating coupler PDL and its bandwidth are included as an extra parameters which leads to extend the Pareto's front to four dimensions. The dependence among the four parameters is reflected in Fig. 4.21.

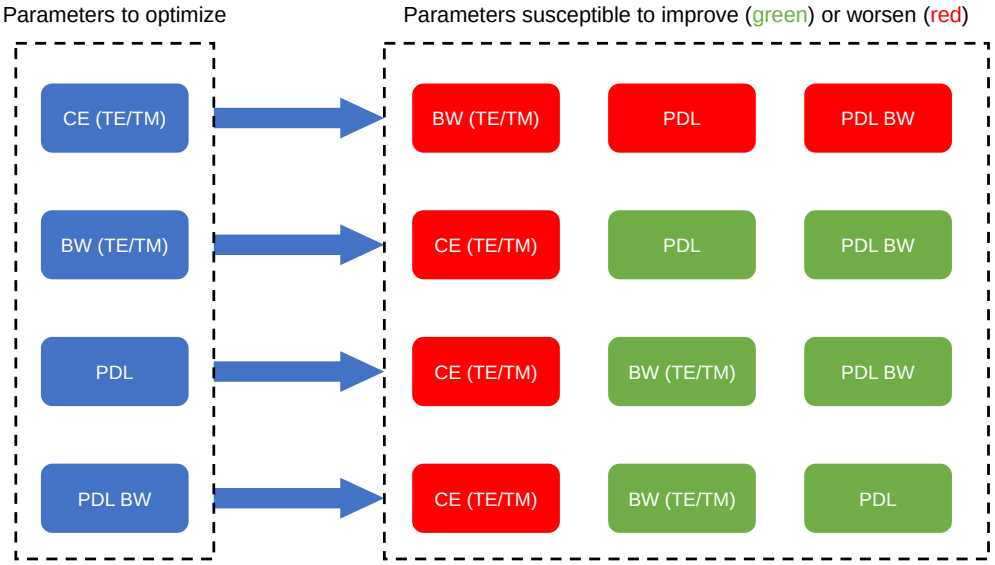

Figure 4.21. Grating coupler parameters dependence.

In this work, grating couplers are designed to cover the telecom C-band (1530 - 1560 nm) while maximizing the coupling efficiency at 1550 nm. The perfect grating does not exist, thus according to Fig. 4.21 three different FOMs are proposed depending on the critical parameter to improve while the others can be relaxed. The first FOM includes the four parameters [Eq. (4.26)] and tries to balance them. The second one is focused on the coupling efficiency and both PDL and bandwidth constraint are relaxed [Eq. (4.27)]. Finally, the last FOM relaxes the performance at 1550 nm and aims to cover the entire C-band with PDLs lower than 1 dB [Eq. (4.28)]. The values of PDL and CE are in dB and are obtained at 1550 nm whereas the bandwidth is in nanometres and is clipped in the C-band wavelength range (35 nm).

$$FOM = \frac{35}{BW^{PDL}} PDL - \frac{35}{BW^{TE}} CE^{TE} - \frac{35}{BW^{TM}} CE^{TM} \tag{4.26}$$

$$FOM = -\left(CE^{TE} + CE^{TM}\right) \max\left(1, PDL\right) \tag{4.27}$$

$$FOM = -\left(CE^{TE} + CE^{TM}\right)\left(\frac{35}{BW^{PDL}}\right)^{8} \tag{4.28}$$

4.5.3 Integration with a Commercial Software

The PSO algorithm is developed in C# using the Visual Studio IDE [58] and is integrated with the RSoft commercial software [59] which is used to calculate the response of the gratings by 2D-FDTD (see Appendix A.3 for grating's simulation method). The developed program is mainly based on variables such as structs, lists and arrays. Several functions have been developed to implement functionalities such as to launch or read the status of RSoft, sorting, search, read/create files, etc. Furthermore, the program works with asynchronous tasks and a user interface was developed to ease its utilization.

User interface

The user interface of the program is shown in Fig. 4.22. The output textbox contains the name of the name of the output simulation. The Nequiv textbox refers to a text file containing the subwavelength fill-factor, the equivalent refractive index of the subwavelength structure and the associated effective refractive index of the slab waveguide for TE and TM polarization. In the Grating Parameters box the user can set the number of periods and the lower- and upper-limits of f_{SWG} and Γ. The Particle Swarm Optimization box contains the parameters related to the PSO algorithm together with elapsed time of the optimization. Finally, at the bottom, a live log indicates the key parameters of each particle and the associated cost (FOM).

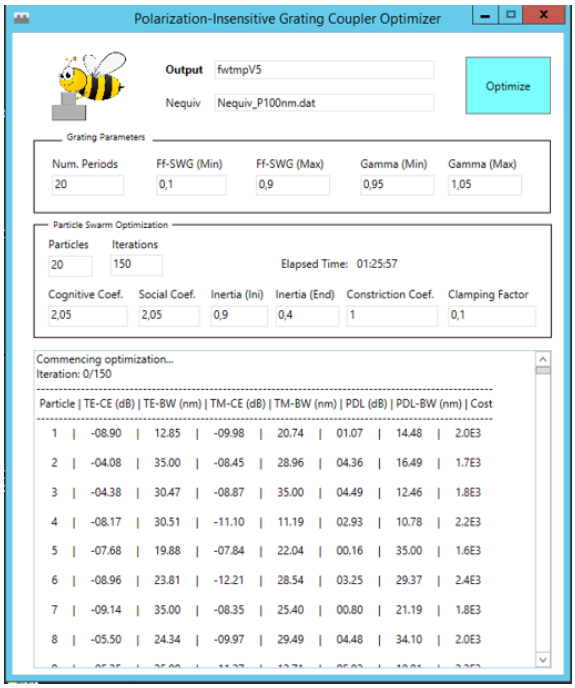

Figure 4.22. User interface of the developed program for combining PSO and RSoft.

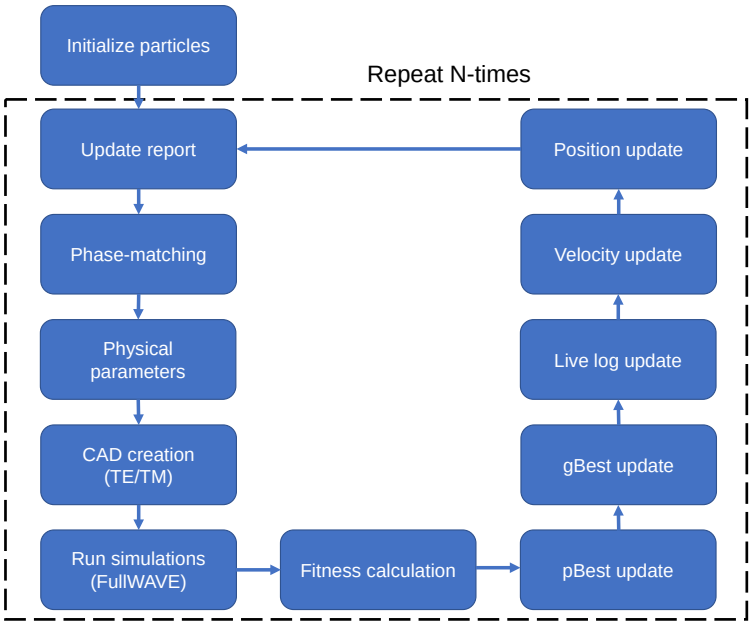

Figure 4.23. Implemented program flow-chart.

Back-end

Once the Optimize button is pressed, the programs begins to run and loads the user parameters as well as the data from the Nequiv file. Then, several steps are carried out internally by the program as depicted in the flow-chart of Fig. 4.23. Detailed description of each step is as follows.

Initialize particles The particles position are randomly initialized. The associated pBests are assigned to that position and velocities are set to zero. The gBest is initialized with a cost equal to $+\infty$.

Update report A text file that serves as report for the user is updated with all the particles position, velocity, pBests and gBest.

Phase-matching The parameters of the grating unit cells (Λ and f) are obtained by using Eqs. (4.19) and (4.20).

Physical parameters The physical parameters such as the widths and the position in the z-axis of the grating etched regions together are set with the associated equivalent refractive index for both polarizations.

CAD creation The CAD files used for simulation by RSoft for TE and TM polarization are created using the aforementioned physical parameters. Furthermore, several fibre monitors are placed over the z-axis in order to obtain the position of the fibre corresponding to the best FOM value in a single simulation.

Run simulations Parallel simulations are launched taking advantage of the CPU multi-cores. The program remains in this step until all the simulations are finished.

Fitness calculation The values of the FOMs are obtained from the output spectra given by ended simulations. For each particle the FOM is calculated at each fibre position and the best is saved.

pBest update The pBests of each particle are updated, if required.

gBest update The gBest is updated, if required.

Live log update The live log of the program is updated with the new values.

Save best spectra The spectra associated to the gBest is saved in text file.

Velocitiy update The velocity of the particles is updated. Clamping is made, if required.

Position update The position of the particles is update with the obtained velocity.

4.6 Final Designs

In this section the results obtained by applying PSO for the different FOMs are shown. Table 4.1 shows the parameters used for all optimization cases and in all cases the number of periods in the grating was fixed to 20. For the three different FOMs the final grating and optimized variables value are summarized as well as the initial and final spectra of the gBest and the evolution of the fitness with the iterations. Finally, a comparison among the three FOMs is carried out.

Table 4.1. Summary of the PSO parameters used for optimization.

Iterations	# Particles	c_1	c_2	ω_{ini}	ω_{end}	k	χ
150	25	2.05	2.05	0.9	0.4	0.1	1

Figure of Merit #1

The best values for the optimized variables together with the corresponding grating's physical parameters are shown in Table 4.2. Most of f_{SWG} values are between 35 % (35 nm) and 75 % (75 nm). On the other hand, the Γ factors are close but different to 1, which proves the necessity of their inclusion in the phase-matching equation and the optimization. Furthermore, for the three variables, most of values are far from boundaries. Regarding, the physical values, the length of the different subwavelength

Table 4.2. Final grating and PSO parameters using FOM #1.

	Grating period																			
	#1	#2	#3	#4	#5	#6	#7	#8	#9	#10	#11	#12	#13	#14	#15	#16	#17	#18	#19	#20
Λ (nm)	742	693	714	723	633	798	601	692	728	598	840	762	575	801	739	662	643	650	662	569
f (%)	60	45	52	48	31	59	17	41	44	19	67	53	21	56	48	36	32	31	40	12
f_{SWG} (%)	37	49	51	64	75	63	82	73	71	84	59	64	10	72	68	72	77	67	47	81
Γ^{TE}	1.02	1.01	0.99	1.01	0.99	1.02	1.02	1.01	1.04	1.01	1.02	1.03	1.03	1.04	1.03	1.00	1.00	1.02	1.00	1.00
Γ^{TM}	0.99	1.02	0.97	0.99	0.99	0.97	1.05	0.99	1.01	1.02	0.96	0.99	1.03	0.98	1.00	0.99	0.99	1.04	1.03	1.04

structures is greater than 100 nm, which is far from the lithography minimum feature size.

The evolution of the gBest fitness as a function of the iterations is shown in Fig. 4.24a. The cost of the gBest is rapidly decreased in the first iterations. This behaviour is attributed to the size of the swarm and the promotion of the exploration. Afterwards, the cost decrease with a slower pace and converges from the 100-iteration. The spectra for the gBest particle at the beginning and at the end of the optimization are depicted in Fig. 4.24b and 4.24c, respectively. At the beginning, the PDLs are very low but because of the low coupling efficiency for both polarizations (see Fig. 4.21). For the final spectra, the coupling efficiencies are increased from -7.5 dB to -4 dB while keeping the PDL lower to 1 dB in the entire C-band.

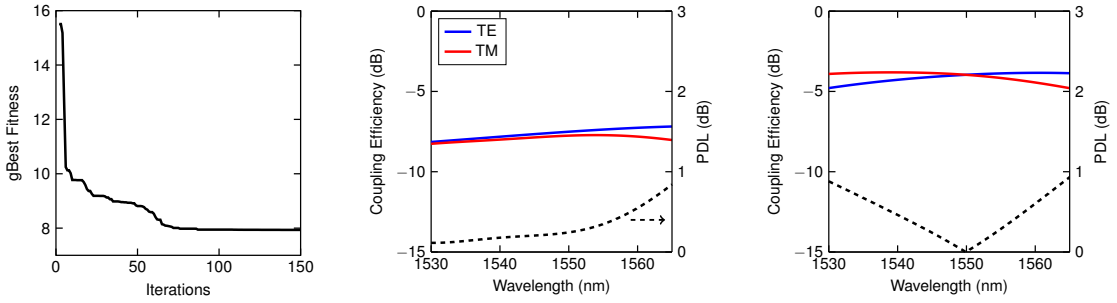

(a) **(b)** **(c)**

Figure 4.24. (a) Fitness of the gBest as a function of the iterations. **(b)** Initial and **(c)** final spectra of the gBest. Results correspond to FOM #1.

Figure of Merit #2

For the second FOM the best values are summarized in Table 4.3. The optimized variables show similar behaviour like the previous design but with different values. Furthermore, the physical parameters are feasible to fabricate since the minimum size is 20 nm.

The PSO converges in the first iterations as seen in Fig. 4.25a. The initial spectrum does not meet the requirement of having less than 1 dB of PDL at 1550 nm. Moreover, the coupling efficiencies are quite low (see Fig. 4.25b). These values are improved at the end of the optimization (see Fig. 4.25c). The PDL is lower than 1 dB, however, the PDL bandwidth is small it was object of optimization since it is not included in the FOM.

Table 4.3. Final grating and PSO parameters using FOM #2.

	Grating period																			
	#1	#2	#3	#4	#5	#6	#7	#8	#9	#10	#11	#12	#13	#14	#15	#16	#17	#18	#19	#20
Λ (nm)	760	700	794	677	650	699	729	669	680	763	718	678	662	796	727	709	610	668	614	743
f (%)	67	51	59	39	33	41	45	37	43	63	49	43	47	59	51	48	26	51	48	55
f_{SWG} (%)	31	45	51	70	75	70	70	73	65	38	63	54	28	53	55	58	68	30	19	48
Γ^{TE}	1.03	0.99	1.04	1.00	1.00	1.02	1.04	1.00	0.98	1.02	1.00	0.99	1.01	1.05	1.01	1.00	0.98	1.00	0.98	1.01
Γ^{TM}	0.98	0.98	1.01	0.99	0.99	1.00	1.01	0.99	0.97	0.98	0.97	1.00	1.01	1.01	0.99	0.98	1.02	0.99	0.96	0.99

Regarding the coupling efficiencies, these suffer an increment of up to 5 dB and values as high as -2.5 dB are achieved for TE polarization.

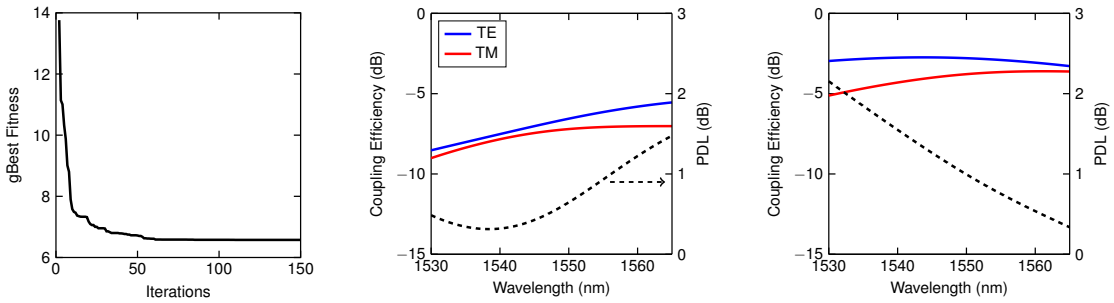

(a) **(b)** **(c)**

Figure 4.25. (a) Fitness of the gBest as a function of the iterations. **(b)** Initial and **(c)** final spectra of the gBest. Results correspond to FOM #2.

Figure of Merit #3

The best values corresponding to the last FOM are summarized in Table 4.4. As well as with the previous designs, the optimized variables are within boundaries and the physical parameters are feasible to fabricate since the minimum size is 20 nm.

Table 4.4. Final grating and PSO parameters using FOM #3.

	Grating period																			
	#1	#2	#3	#4	#5	#6	#7	#8	#9	#10	#11	#12	#13	#14	#15	#16	#17	#18	#19	#20
Λ (nm)	696	652	763	781	644	626	713	695	803	701	677	653	634	655	620	541	679	712	573	665
f (%)	60	43	63	55	28	32	45	41	61	41	50	37	37	43	38	6	44	51	13	39
f_{SWG} (%)	30	43	41	60	77	77	71	71	57	67	32	49	42	33	18	84	42	42	83	57
Γ^{TE}	0.98	0.97	1.00	1.04	1.02	0.97	1.01	1.01	1.03	1.03	1.00	1.00	0.98	1.00	1.03	0.98	1.01	1.02	1.00	0.99
Γ^{TM}	0.95	0.99	0.96	1.00	1.03	0.96	0.98	0.99	0.98	1.02	1.00	1.04	1.02	1.03	1.03	1.03	1.03	1.01	1.04	1.01

The PSO converges in in a similar way as in FOM #1 as seen in Fig. 4.26a. Although the initial spectrum meets the requirement of having a PDL bandwidth in the C-band with PDLs lower than 1 dB, the coupling efficiencies are very low (see Fig. 4.26b). After

the optimization, PDL requirements are still met but coupling efficiencies improve more than 5 dB as shown in 4.25c.

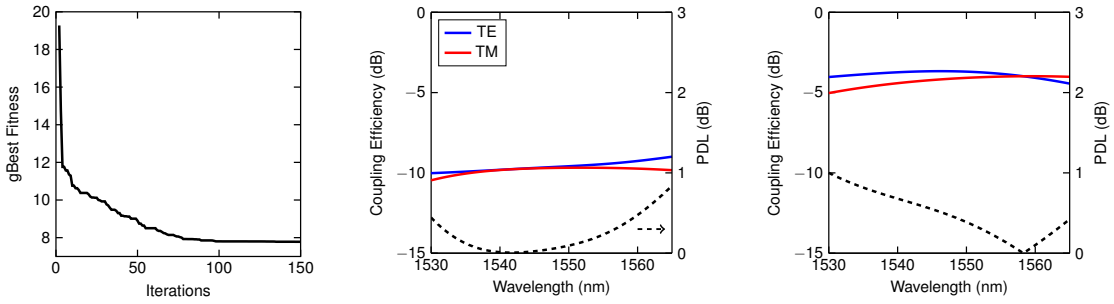

(a) **(b)** **(c)**

Figure 4.26. (a) Fitness of the gBest as a function of the iterations. **(b)** Initial and **(c)** final spectra of the gBest. Results correspond to FOM #3.

4.6.1 Comparison

The final parameters of the gratings for the different FOMs are shown in Table 4.5. Overall, the best grating performance is achieved to the grating corresponding to FOM #1. The grating of FOM #2 presents better CE for TE polarization, but at the cost of lower bandwidth and an increase in the PDL. Finally, the grating of FOM #3 covers the entire C-band with PDL lower than 1 dB, but with slightly worse CE values than the one of FOM #1 since this parameter it is not evaluated in the FOM.

Table 4.5. Comparison of the final gratings performance. Coupling efficiencies and PDLs are given at $\lambda = 1550$ nm.

	TE		TM		PDL	
	CE (dB)	BW (nm)	CE (dB)	BW (nm)	PDL (dB)	BW (nm)
FOM #1	-3.96	35.0	-3.97	35.0	0.01	35.0
FOM #2	-2.79	35.0	-3.78	29.06	0.99	21.3
FOM #3	-3.70	35.0	-4.08	34.4	0.39	35.0

It would be also interesting to known if by using other simulation methods or doing a parametric scan of the optimized variables, similar results would have been attained. A comparison in terms of time and resources among the different FDTD methods to simulate a grating coupler is shown in Table 4.6. The comparison is made for the same workstation that has 8 core CPU @ 3.00 GHz (Intel Xeon E5450) and 18 Gb of RAM. Simulate the whole structure by mean of 3D-FDTD is feasible but becomes very low efficient. Periodic boundary conditions (PBC) can be applied because of the subwavelength periodicity in the x-axis. By using this condition, the times decreases from around one day to one hour. However, despite this drastic decrease, optimization is not feasible

yet. Although PSO converges rapidly, if the same optimization produce is applied simulating the gratings with 3D-FDTD with PBC then, the optimization would last almost 64 years. Finally, by simulating the cross-section of the grating with 2D-FDTD, simulation time decreases to only 20 s with a single core of the CPU. This last enables to simulate different gratings at the same time. As a consequence, the total optimization time is only 6-7 hours.

Table 4.6. Grating simulation for different FDTD methods.

	3D-FDTD	3D-FDTD (PBC)	2D-FDTD
Time	$\sim$ 24 h	$\sim$ 1 h	$\sim$ 20 s
CPU Cores	8	8	1
RAM	$\sim$ 12 Gb	$\sim$ 800 Mb	$\sim$ 20 Mb

On the other hand, let us suppose a very coarse parametric scan of the grating coupler parameters with 10 steps for each variable. The number of combinations is 10^{60} and gratings are simulated with 2D-FDTD and taking advantage of parallel simulations. The required time would be of $\sim 5 \times 10^{54}$ years. The number of workstations working on clustering to reduce the total time to 6 hours would be $\sim 10^{56}$, which assuming that each workstation consumes 400 W this would be equal to the power that generates $\sim 10^{32}$ Suns [60]. In other words, it is impossible to apply a parametric scan to all the variables for optimization purposes.

Chapter 5

Conclusions and Future Work

In this master thesis, novel high-performance polarization-insensitive grating couplers have been proposed for the silicon photonics platform. The working principle of the proposed gratings is two-fold. On one hand, the polarization-insensitive condition is provided by using subwavelength structures that act as uniaxial dielectric homogeneous metamaterials. On the other hand, the high-performance behaviour is achieved after optimizing the grating by means of a nature-inspired algorithm such as particle swarm optimization.

The investigation of the influence of the subwavelength pitch has been focused on the capability of approximating these kind of structures as homogenous materials. Different studies have been carried out through: (i) the analysis of the dispersion-relation equation; (ii) the field profile and axial ratio; (iii) the leaky modes and transmittance/reflectance values when it is interfaced with silicon. From (i) it has been shown that diffraction or higher-order solutions are suppressed from pitches lower to 450 nm. From (ii) the field profile is not constant along the periodicity and approximates to a plane wave when $\Lambda_{SWG} \rightarrow 0$ nm. This field variation arise leaky modes when the structure is interfaced with silicon, as it has been shown in (iii). For Λ_{SWG} values greater than 100 nm, these leaky modes could interfere with the propagated wave within the grating and thus, the homogeneity approximation does not fulfil for the crosswise stack. Furthermore, for TE polarization the equivalent metamaterial exhibits not only a uniaxial dielectric behaviour but also a diamagnetic one. Therefore, pitch values lower than $\sim$ 100 nm are needed to accurately approximate the periodic structure as a pure dielectric homogenous material.

Regarding the optimization, the combination of the developed program integrated with the commercial photonic software (RSoft) –the first to implement the PSO and the second to perform the simulations– has provided excellent results. The potential of the algorithm has been tested with different grating specifications defined in the FOM. In all cases, the achieved results have met the specifications with values comparable or even superior to the state-of-the-art. Furthermore, the utilization of this algorithm together with the approximation of the dielectric metamaterials as homogenous –that allows fast 2D-FDTD simulations– provides an ultra-efficient design method compared with typical parametric scans of the grating variables.

Therefore, PSO has been successfully demonstrated as an efficient way for optimizing complex and high-degree freedom photonic structures such as these metamaterial grating couplers. The drastic reduction that proves this tool in terms of time and re-

sources would be interesting for the industry where one of the main objectives is cost-saving. On the other hand, the proposed grating designs could be used in a wide range of integrated photonic applications such as telecom or new ways of computing.

Future Work

The topics developed in this thesis allow for future work. More interesting are:

- The experimental demonstration of the proposed gratings would be the last step to close this work. The gratings could be fabricated using PECVD for depositing the 100 nm remaining silicon layer and the 1-μm-thick SiO_2 upper-cladding. For lithography of the grating patterns electron beam lithography (EBL) would be used.
- The study of subwavelength structures have arisen intriguing results that would be interesting to further investigate. The diamagnetic response that exhibits the equivalent metamaterial for TE polarization is very strong –comparable to superconductors – and, to the best of our knowledge, have not been reported up to date this kind of behaviour using lossless dielectric structures.
- Finally, regarding the PSO, the developed software allows for further improvements such as including more features that improve the user experience. Furthermore, the software could be extended to any kind of grating and integrated photonic platform.

Concluding Remarks

I would like to highlight all of the bulk work that has been carried out to perform this thesis. Most of this work has been developed based on mathematical formulae and expressions. These have to be translated into a computer program or script in which many times either the formal definition cannot be implemented, or the intrinsic discretization of the expression arise other issues that have to be tackle. Continuing with programming, implementing PSO and integrating with RSoft have required thousands of code lines and countless time of debugging process. Although RSoft is very well documented and their files can be modified easily, it has to be noticed that is not an open source program. Indeed, a wide variety of programs –each one with its own learning curve– have been used to develop (Visual Studio, Matlab, Mathematica, RSoft...) and write (LaTeX, PowerPoint, Adobe Acrobat, Mendeley, Blender...) this thesis.

Author's Merits

The potential of PSO applied to polarization-intensive grating couplers based on dielectric metamaterials was presented at the 19^{th} European Conference of Integrated Optics (ECIO)[1] as an oral talk:

- **J. Parra** and P. Sanchis, "Particle Swarm Optimization for Polarization-Independent and Low Loss Grating Couplers," in 19^{th} *European Conference of Integrated Optics (ECIO 2017)*, pp. 1-3, Belgium, 2017.

Although it is not directly related to this work, the study of the effective medium theory for the subwavelength structures allowed its application on a hybrid silicon/-vanadium dioxide waveguide that act as a TE pass-polariser. This work was published in the journal *Optics Letters*:

- L. D. Sánchez, I. Olivares, **J. Parra**, M. Menghini, P. Homm, J.-P. Locquet, and P. Sanchis, "Experimental demonstration of a tunable transverse electric pass polarizer based on hybrid VO_2/silicon technology," *Optics Letters*, vol. 43, no. 15, p. 3650, 2018.

[1] ECIO is a conference focused on leading edge research on integrated optics, optoelectronics and nanophotonics and gathers experts from academia and industry to show their latest technical results, and showcase their products and services [www.ecio-conference.org].

Bibliography

[1] V. Marx, "The big challenges of big data," *Nature*, vol. 498, no. 7453, pp. 255–260, 2013.

[2] A. Lord, A. Soppera, and A. Jacquet, "The impact of capacity growth in national telecommunications networks," *Philosophical Transactions of the Royal Society A: Mathematical, Physical and Engineering Sciences*, vol. 374, no. 2062, 2016.

[3] P. J. Winzer and D. T. Neilson, "From Scaling Disparities to Integrated Parallelism: A Decathlon for a Decade," *Journal of Lightwave Technology*, vol. 35, no. 5, pp. 1099–1115, 2017.

[4] P. J. Winzer, D. T. Neilson, and A. R. Chraplyvy, "Fiber-optic transmission and networking: the previous 20 and the next 20 years [Invited]," *Optics Express*, vol. 26, no. 18, p. 24190, 2018.

[5] P. Dong, Y. K. Chen, G. H. Duan, and D. T. Neilson, "Silicon photonic devices and integrated circuits," *Nanophotonics*, vol. 3, no. 4-5, pp. 215–228, 2014.

[6] R. Soref, "The past, present, and future of silicon photonics," *IEEE Journal on Selected Topics in Quantum Electronics*, vol. 12, no. 6, pp. 1678–1687, 2006.

[7] Z. Fang and C. Z. Zhao, "Recent Progress in Silicon Photonics: A Review," *ISRN Optics*, vol. 2012, pp. 1–27, 2012.

[8] Yole, "Silicon Photonics and Photonic Integrated Circuits 2019," Tech. Rep., 2019.

[9] J. Wang, F. Sciarrino, A. Laing, and M. G. Thompson, "Integrated photonic quantum technologies," 2019.

[10] J. Feldmann, N. Youngblood, C. D. Wright, H. Bhaskaran, and W. H. Pernice, "All-optical spiking neurosynaptic networks with self-learning capabilities," *Nature*, vol. 569, no. 7755, pp. 208–214, 2019.

[11] A. H. Atabaki, S. Moazeni, F. Pavanello, H. Gevorgyan, J. Notaros, L. Alloatti, M. T. Wade, C. Sun, S. A. Kruger, H. Meng, K. A. Qubaisi, I. Wang, B. Zhang, A. Khilo, C. V. Baiocco, M. A. Popović, V. M. Stojanović, and R. J. Ram, "Integrating photonics with silicon nanoelectronics for the next generation of systems on a chip," *Nature*, vol. 560, no. 7716, 2018.

[12] P. Henzi, D. G. Rabus, K. Bade, U. Wallrabe, and J. Mohr, "Low-cost single-mode waveguide fabrication allowing passive fiber coupling using LIGA and UV

flood exposure," *Micro-Optics: Fabrication, Packaging, and Integration*, vol. 5454, no. September, p. 64, 2004.

[13] P. M. Hill, R. Olshansky, and W. K. Burns, "Optical Polarization Division Multiplexing at 4 Gb/s," *IEEE Photonics Technology Letters*, vol. 4, no. 5, pp. 500–502, 1992.

[14] W. Bogaerts, D. Taillaert, P. Dumon, D. Van Thourhout, R. Baets, and E. Pluk, "A polarization-diversity wavelength duplexer circuit in silicon-on-insulator photonic wires," *Optics Express*, vol. 15, no. 4, p. 1567, 2007.

[15] X. Chen and H. K. Tsang, "Polarization-independent grating couplers for silicon-on-insulator nanophotonic waveguides," *Optics Letters*, vol. 36, no. 6, p. 796, 2011.

[16] Z. Cheng and H. K. Tsang, "Experimental demonstration of polarization-insensitive air-cladding grating couplers for silicon-on-insulator waveguides," *Optics Letters*, vol. 39, no. 7, p. 2206, 2014.

[17] J. H. Song, F. E. Doany, A. K. Medhin, N. Dupuis, B. G. Lee, and F. R. Libsch, "Polarization-independent nonuniform grating couplers on silicon-on-insulator," *Optics Letters*, vol. 40, no. 17, p. 3941, 2015.

[18] J. Zhang, J. Yang, H. Lu, W. Wu, J. Huang, and S. Chang, "Subwavelength TE/TM grating coupler based on silicon-on-insulator," *Infrared Physics and Technology*, vol. 71, pp. 542–546, 2015.

[19] J. Parra and P. Sanchis, "Particle Swarm Optimization for Polarization-Independent and Low Loss Grating Couplers," in *19th European Conference on Integrated Optics*, 2017, pp. 1–3.

[20] D. Taillaert, F. Van Laere, M. Ayre, W. Bogaerts, D. Van Thourhout, P. Bienstman, and R. Baets, "Grating couplers for coupling between optical fibers and nanophotonic waveguides," *Japanese Journal of Applied Physics, Part 1: Regular Papers and Short Notes and Review Papers*, vol. 45, no. 8 A, pp. 6071–6077, 2006.

[21] Y. Ding, C. Peucheret, and H. Ou, "Ultra-high-efficiency apodized grating coupler using a fully etched photonic crystal," *Opt. Lett.*, vol. 38, no. 15, pp. 2732–2734, 2013.

[22] Y. Wang, X. Wang, J. Flueckiger, H. Yun, W. Shi, R. Bojko, N. A. F. Jaeger, and L. Chrostowski, "Focusing sub-wavelength grating couplers with low back reflections for rapid prototyping of silicon photonic circuits," *Optics Express*, vol. 22, no. 17, p. 20652, 2014.

[23] D. Taillaert, "Grating couplers as Interface between Optical Fibres and Nanophotonic Waveguides," Ph.D. dissertation, 2005.

[24] D. Vermeulen, S. Selvaraja, P. Verheyen, G. Lepage, W. Bogaerts, P. Absil, D. Van Thourhout, and G. Roelkens, "High-efficiency fiber-to-chip grating couplers realized using an advanced CMOS-compatible Silicon-On-Insulator platform," *Optics Express*, vol. 18, no. 17, p. 18278, 2010.

[25] J. Jian, P. Xu, H. Chen, M. He, Z. Wu, L. Zhou, L. Liu, C. Yang, and S. Yu, "High-efficiency hybrid amorphous silicon grating couplers for sub-micron-sized lithium niobate waveguides," *Optics Express*, vol. 26, no. 23, p. 29651, 2018.

[26] C. Alonso-Ramos, A. Ortega-Moñux, Í. Molina-Fernández, P. Cheben, L. Zavargo-Peche, and R. Halir, "Efficient fiber-to-chip grating coupler for micrometric SOI rib waveguides," *Optics Express*, vol. 18, no. 14, pp. 15 189–15 200, 2010.

[27] R. Halir, P. J. Bock, P. Cheben, A. Ortega-Moñux, C. Alonso-Ramos, J. H. Schmid, J. Lapointe, D. X. Xu, J. G. Wangüemert-Pérez, Í. Molina-Fernández, and S. Janz, "Waveguide sub-wavelength structures: A review of principles and applications," *Laser and Photonics Reviews*, vol. 9, no. 1, pp. 25–49, 2015.

[28] P. Cheben, R. Halir, J. H. Schmid, H. A. Atwater, and D. R. Smith, "Subwavelength integrated photonics," *Nature*, vol. 560, no. 7720, pp. 565–572, 2018.

[29] P. Yeh, A. Yariv, and C.-s. Hong, "Electromagnetic propagation in periodic stratified media. I. General theory*," *J. Opt. Soc. Am.*, vol. 67, no. 4, pp. 423–438, 1977.

[30] R.-B. R. Hwang, *Periodic Structures Periodic Structures Mode-Matching Approach and Applications in*, J. Wiley, Ed. John Wiley & Sons, Ltd, 2013.

[31] C. Gu and P. Yeh, "Form birefringence dispersion in periodic layered media." *Optics letters*, vol. 21, no. 7, pp. 504–6, 1996.

[32] G. A. Niklasson, C. G. Granqvist, and O. Hunderi, "Effective medium models for the optical properties of inhomogeneous materials," *Applied Optics*, vol. 20, no. 1, p. 26, 1981.

[33] P. U. Jepsen, B. M. Fischer, A. Thoman, H. Helm, J. Y. Suh, R. Lopez, and R. F. Haglund, "Metal-insulator phase transition in a V O2 thin film observed with terahertz spectroscopy," *Physical Review B - Condensed Matter and Materials Physics*, vol. 74, no. 20, pp. 1–9, 2006.

[34] L. D. Sánchez, I. Olivares, J. Parra, M. Menghini, P. Homm, J.-P. Locquet, and P. Sanchis, "Experimental demonstration of a tunable transverse electric pass polarizer based on hybrid VO 2 /silicon technology," *Optics Letters*, vol. 43, no. 15, p. 3650, 2018.

[35] S. M. Rytov, "Electromagnetic properties of a finely stratified medium," *Soviet Physics JETP*, vol. 2, no. 3, pp. 446–475, 1956.

[36] D. H. Raguin and G. M. Morris, "Antireflection structured surfaces for the infrared spectral region," *Applied Optics*, vol. 32, no. 7, p. 1154, 1993.

[37] H. Kikuta, H. Yoshida, and K. Iwata, "Ability and limitation of effective medium theory for subwavelength gratings," *Optical Review*, vol. 2, no. 2, pp. 92–99, 1995.

[38] S. Tang, B. Zhu, M. Jia, Q. He, S. Sun, Y. Mei, and L. Zhou, "Effective-medium theory for one-dimensional gratings," *Physical Review B - Condensed Matter and Materials Physics*, vol. 91, no. 17, pp. 1–10, 2015.

[39] P. Bienstman, "Rigorous and efficient modelling of wavelength scale photonic components," Ph.D. dissertation, 2001.

[40] Mathworks, "MATLAB," 2019. [Online]. Available: https://es.mathworks.com/products/matlab.html

[41] J. M. Luque-González, A. Herrero-Bermello, A. Ortega-Moñux, Í. Molina-Fernández, A. V. Velasco, P. Cheben, J. H. Schmid, S. Wang, and R. Halir, "Tilted subwavelength gratings: controlling anisotropy in metamaterial nanophotonic waveguides," *Optics Letters*, vol. 43, no. 19, p. 4691, 2018.

[42] J. Parra Gómez, *Desarrollo de la tecnología de silicio amorfo para aplicaciones fotónicas*, dec 2016.

[43] W. Chen and H. Ahmed, "Fabrication of 5-7 nm wide etched lines in silicon using 100 keV electron-beam lithography and polymethylmethacrylate resist," *Applied Physics Letters*, vol. 62, no. 13, pp. 1499–1501, 1993.

[44] M. M. Mirza, P. Velha, G. Ternent, H. P. Zhou, K. E. Docherty, and D. J. Paul, "Silicon nanowire devices with widths below 5 nm," *Proceedings of the IEEE Conference on Nanotechnology*, no. August, 2012.

[45] S. Sengupta, S. Basak, and R. Peters, "Particle Swarm Optimization: A Survey of Historical and Recent Developments with Hybridization Perspectives," *Machine Learning and Knowledge Extraction*, vol. 1, no. 1, pp. 157–191, 2018.

[46] M. Djavid, S. A. Mirtaheri, and M. S. Abrishamian, "Photonic crystal notch-filter design using particle swarm optimization theory and finite-difference time-domain analysis," *Journal of the Optical Society of America B*, vol. 26, no. 4, p. 849, 2009.

[47] Y. Zhang, S. Yang, A. E.-J. Lim, G.-Q. Lo, C. Galland, T. Baehr-Jones, and M. Hochberg, "A compact and low loss Y-junction for submicron silicon waveguide," *Optics Express*, vol. 21, no. 1, p. 1310, 2013.

[48] B. Shen, R. Polson, and R. Menon, "Increasing the density of passive photonic-integrated circuits via nanophotonic cloaking," *Nature Communications*, vol. 7, pp. 1–9, 2016.

[49] M. Shokooh-saremi and R. Magnusson, "the Design of Diffraction Grating Filters," *Optics Letters*, vol. 32, no. 8, pp. 894–896, 2007.

[50] G. Roelkens, D. Vermeulen, D. Van Thourhout, R. Baets, S. Brision, P. Lyan, P. Gautier, and J. M. Fdli, "High efficiency diffractive grating couplers for interfacing a single mode optical fiber with a nanophotonic silicon-on-insulator waveguide circuit," *Applied Physics Letters*, vol. 92, no. 13, pp. 2–4, 2008.

[51] B. Wohlfeil, L. Zimmermann, and K. Petermann, "Optimization of fiber grating couplers on SOI using advanced search algorithms," *Optics Letters*, vol. 39, no. 11, p. 3201, 2014.

[52] Y. Wang, X. Wang, J. Flueckiger, H. Yun, W. Shi, R. Bojko, N. A. F. Jaeger, and L. Chrostowski, "Focusing sub-wavelength grating couplers with low back reflections for rapid prototyping of silicon photonic circuits," *Optics Express*, vol. 22, no. 17, p. 20652, 2014.

[53] Q. Zhong, V. Veerasubramanian, Y. Wang, W. Shi, D. Patel, S. Ghosh, A. Samani, L. Chrostowski, R. Bojko, and D. V. Plant, "Focusing-curved subwavelength grating couplers for ultra-broadband silicon photonics optical interfaces," *Optics Express*, vol. 22, no. 15, p. 18224, 2014.

[54] Y. Wang, H. Yun, Z. Lu, R. Bojko, W. Shi, X. Wang, J. Flueckiger, F. Zhang, M. Caverley, N. A. Jaeger, and L. Chrostowski, "Apodized focusing fully etched subwavelength grating couplers," *IEEE Photonics Journal*, vol. 7, no. 3, pp. 1–10, 2015.

[55] M. Passoni, D. Gerace, L. Carroll, and L. C. Andreani, "Simultaneous optimization of coupling efficiency and bandwidth of waveguide grating couplers," in *16th European Conference on Integrated Photonics*, 2016, pp. 1–2.

[56] A. P. Engelbrecht, *Computational intelligence: An introduction*, J. Wiley, Ed. John Wiley & Sons, Ltd, 2007.

[57] X. B. Hu, M. Wang, and E. Di Paolo, "Calculating complete and exact pareto front for multiobjective optimization: A new deterministic approach for discrete problems," *IEEE Transactions on Cybernetics*, vol. 43, no. 3, pp. 1088–1101, 2013.

[58] Microsoft, "Microsoft Visual Studio," 2017. [Online]. Available: https://visualstudio.microsoft.com/es/vs/

[59] Synopsys, "RSoft," 2019. [Online]. Available: https://www.synopsys.com/photonic-solutions/rsoft-photonic-device-tools.html

[60] D. R. Williams, "Sun Fact Sheet," 2018. [Online]. Available: https://nssdc.gsfc.nasa.gov/planetary/factsheet/sunfact.html

Appendices

Appendix A

Numerical Simulation Methods

Throughout the present work, several numerical simulations have been carried in order to solve the Maxwell's equations either by using finite element method (FEM) or finite-difference time-domain (FDTD). This appendix deals with the set-up simulations parameters such as boundary conditions or mesh size used in the different simulation of the structures used in the work.

A.1 Eigenmodes of a Slab Waveguide

Eigenmodes of a slab waveguide are obtained by 1D-FEM since the refractive index varies only in the y-axis. The simulation domain is depicted in Fig. A.1. A silicon waveguide is surrounded by a 1-µm-thick under- and upper-cladding of SiO_2. However, the silicon can be replaced by other material with refractive index greater than SiO_2. Simulations are carried out at 1550 nm using a mesh size larger than 25 points per wavelength in order to obtain a good accuracy in the refractive index value.

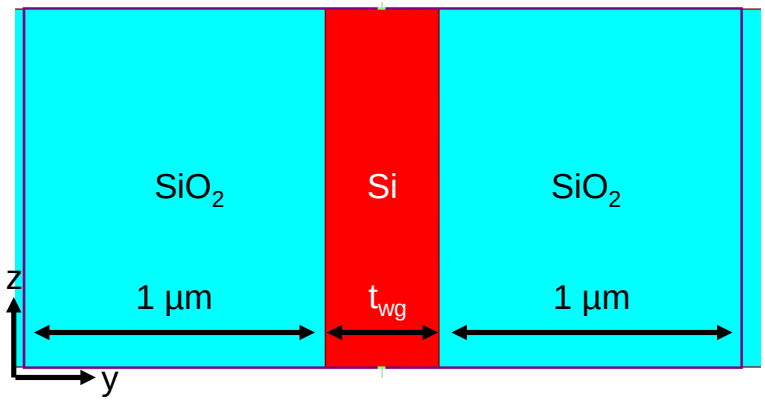

Figure A.1. Slab waveguide simulation set-up.

A.2 Diffraction Strength Between a Silicon Slab Waveguide and a Metamaterial Slab Waveguide

The diffraction strength or coupling losses between a silicon slab waveguide (medium I) and a metamaterial slab waveguide (medium II) is obtained by using 2D-FDTD. In Fig. A.2 is shown the CAD of the simulation set-up. Both slab waveguides are 320-nm-thick and fully surrounded of SiO_2. The permittivity of the core metamaterial waveguide is obtained using Rytov expressions for TE and TM polarization [Eqs. (4.15) and (4.14)]. Perfect match layers (PMLs) are used at boundaries in order to absorb the scattered light at the interface between both waveguides. The structured is excited with the slab mode of the Si-waveguide, which propagated along the z-axis. Finally, the diffraction strength is calculated as the relation between the input power and the remain guided power. This latter is recorded by placing a monitor far away from the interface to avoid leaky waves.

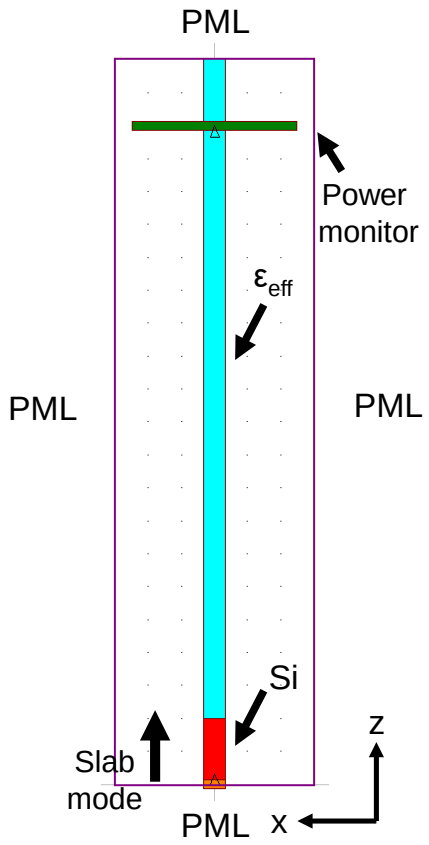

Figure A.2. Simulation set-up used for obtaining the diffraction strength between a Si-slab waveguide and a metamaterial slab waveguide. The thickness of both waveguides is 320 nm and are fully surrounded of SiO_2.

A.3 Grating Coupler Performance

Grating couplers are simulated using 2D-FDTD. The simulation set-up is shown in Fig. A.3. The grating is comprised of a silicon waveguide with metamaterial teeth of a

refractive index Nequiv. The domain comprises the silicon substrate to take into account reflections from the SiO_2-BOX/Si substrate interface. Open boundary conditions are set by using a perfect matched layer (PML). A non-uniform mesh is used in order to alleviate the computational cost while maintaining the accuracy. A maximum size of 50 nm is set with a minimum division of 10 in both axis between refractive index changes. Therefore, the mesh is ultra-fine in the grating teeth while in the air region becomes coarse. A pulse is used as a launch in order to obtain the performance of the grating with a single simulation by using afterwards the fast Fourier transform. Furthermore, several monitors are placed with an offset in the z-axis in order to record the best possible coupling efficiency. This latter is calculated as the overlap between mode of a single-mode fibre and the recorded diffracted wave.

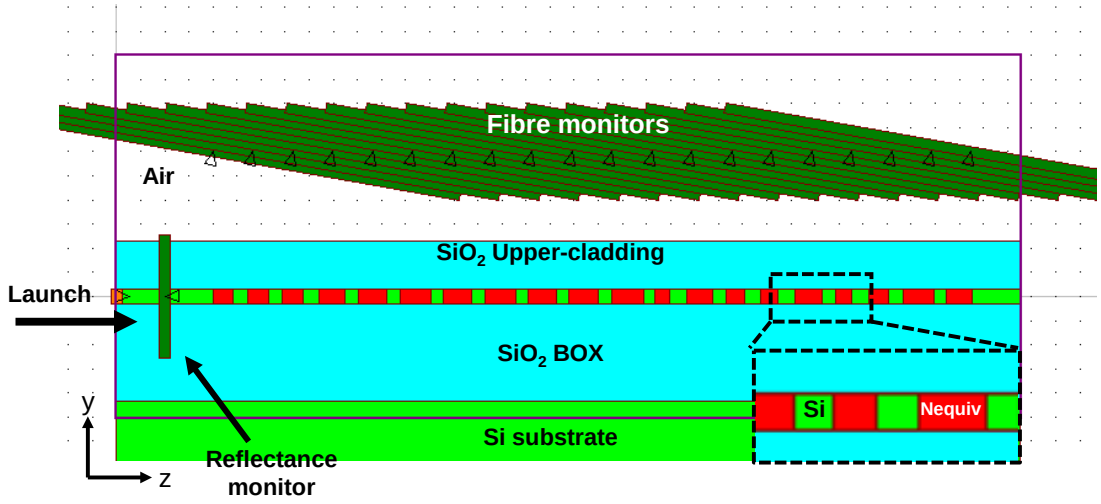

Figure A.3. Simulation set-up used obtaining the performance of the polarization-independent grating couplers.

Appendix B

Transfer Matrix Method applied to Periodic Structures

This appendix deals with the transfer matrix method (TMM) applied to a two-layer crosswise periodic structure. The utilization of TMM allows to obtain both the field profile and propagation constant. Let us suppose a semi-infinite structure in the y- and z-axis formed by two-layers with permittivites ε_a and ε_b with thicknesses a and b, respectively (see Fig. B.1). The two-layers extend periodically in the x-axis with a pitch $\Lambda = a + b$.

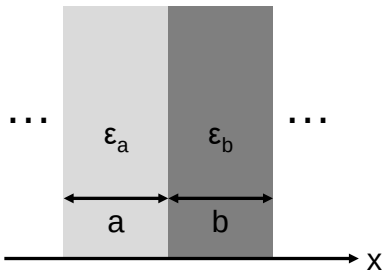

Figure B.1. Two-layers periodic stack.

The field solution, $\phi(x)$, which corresponds to the E- and H-field depending on the polarization, can be expressed in each n-unitary cell as:

$$\begin{aligned} \phi_{a,n}(x) &= a_n^+ e^{-jk_{x,a}(x-n\Lambda)} + a_n^- e^{jk_{x,a}(x-n\Lambda)} \\ \phi_{b,n}(x) &= b_n^+ e^{-jk_{x,b}(x-n\Lambda)} + b_n^- e^{jk_{x,b}(x-n\Lambda)}, \end{aligned} \tag{B.1}$$

where the superscripts $+$ and $-$ stands for the forward $(+x)$ and backward $(-x)$ wave, the subscript n is the n-unitary cell and k_x is the value of the wavevector. On the other hand, the field must satisfy the boundary condition of the continuity of the vector displacement (D) and its derivative at the interfaces. For the E_y-polarized light we have that:

$$\begin{aligned} &\phi_{a,n}(n\Lambda + a) = \phi_{b,n}(n\Lambda + a) \qquad \text{and} \qquad \phi_{b,n}(n\Lambda + \Lambda) = \phi_{a,n+1}(n\Lambda + \Lambda) \\ &\frac{d\phi_{a,n}(n\Lambda + a)}{dx} = \frac{d\phi_{b,n}(n\Lambda + a)}{dx} \qquad \text{and} \qquad \frac{d\phi_{b,n}(n\Lambda + \Lambda)}{dx} = \frac{d\phi_{a,n+1}(n\Lambda + \Lambda)}{dx} \end{aligned} \tag{B.2}$$

whereas for the H_y-polarized light:

$$\phi_{a,n}(n\Lambda + a) = \phi_{b,n}(n\Lambda + a) \qquad \text{and} \qquad \phi_{b,n}(n\Lambda + \Lambda) = \phi_{a,n+1}(n\Lambda + \Lambda)$$

$$\frac{1}{\varepsilon_a}\frac{d\phi_{a,n}(n\Lambda + a)}{dx} = \frac{1}{\varepsilon_b}\frac{d\phi_{b,n}(n\Lambda + a)}{dx} \qquad \text{and} \qquad \frac{1}{\varepsilon_a}\frac{d\phi_{b,n}(n\Lambda + \Lambda)}{dx} = \frac{1}{\varepsilon_b}\frac{d\phi_{a,n+1}(n\Lambda + \Lambda)}{dx} \tag{B.3}$$

Replacing the above expressions into the field expressions and arranging the resulting equations in a matrix form, we arrive to Eqs. (B.4) and (B.5) for E_y-polarized light and Eqs. (B.6) and (B.7) for H_y-polarized light.

$$\begin{pmatrix} 1 & 1 \\ -k_{x,a} & k_{x,a} \end{pmatrix} \begin{pmatrix} e^{-jk_{x,a}a} & 0 \\ 0 & e^{jk_{x,a}a} \end{pmatrix} \begin{pmatrix} a_n^+ \\ a_n^- \end{pmatrix} = \begin{pmatrix} 1 & 1 \\ -k_{x,b} & k_{x,b} \end{pmatrix} \begin{pmatrix} e^{-jk_{x,b}a} & 0 \\ 0 & e^{jk_{x,b}a} \end{pmatrix} \begin{pmatrix} b_n^+ \\ b_n^- \end{pmatrix} \tag{B.4}$$

$$\begin{pmatrix} 1 & 1 \\ -k_{x,a} & k_{x,a} \end{pmatrix} \begin{pmatrix} 1 & 0 \\ 0 & 1 \end{pmatrix} \begin{pmatrix} a_{n+1}^+ \\ a_{n+1}^- \end{pmatrix} = \begin{pmatrix} 1 & 1 \\ -k_{x,b} & k_{x,b} \end{pmatrix} \begin{pmatrix} e^{-jk_{x,b}\Lambda} & 0 \\ 0 & e^{jk_{x,b}\Lambda} \end{pmatrix} \begin{pmatrix} b_n^+ \\ b_n^- \end{pmatrix}. \tag{B.5}$$

$$\begin{pmatrix} 1 & 1 \\ -\frac{k_{x,a}}{\varepsilon_a} & \frac{k_{x,a}}{\varepsilon_a} \end{pmatrix} \begin{pmatrix} e^{-jk_{x,a}a} & 0 \\ 0 & e^{jk_{x,a}a} \end{pmatrix} \begin{pmatrix} a_n^+ \\ a_n^- \end{pmatrix} = \begin{pmatrix} 1 & 1 \\ -\frac{k_{x,b}}{\varepsilon_b} & \frac{k_{x,b}}{\varepsilon_b} \end{pmatrix} \begin{pmatrix} e^{-jk_{x,b}a} & 0 \\ 0 & e^{jk_{x,b}a} \end{pmatrix} \begin{pmatrix} b_n^+ \\ b_n^- \end{pmatrix} \tag{B.6}$$

$$\begin{pmatrix} 1 & 1 \\ -\frac{k_{x,a}}{\varepsilon_a} & \frac{k_{x,a}}{\varepsilon_a} \end{pmatrix} \begin{pmatrix} 1 & 0 \\ 0 & 1 \end{pmatrix} \begin{pmatrix} a_{n+1}^+ \\ a_{n+1}^- \end{pmatrix} = \begin{pmatrix} 1 & 1 \\ -\frac{k_{x,b}}{\varepsilon_b} & \frac{k_{x,b}}{\varepsilon_b} \end{pmatrix} \begin{pmatrix} e^{-jk_{x,b}\Lambda} & 0 \\ 0 & e^{jk_{x,b}\Lambda} \end{pmatrix} \begin{pmatrix} b_n^+ \\ b_n^- \end{pmatrix}. \tag{B.7}$$

For the sake of simplicity this can be expressed as:

$$\boldsymbol{M}_a \boldsymbol{P}_a(a) \begin{pmatrix} a_n^+ \\ a_n^- \end{pmatrix} = \boldsymbol{M}_b \boldsymbol{P}_b(a) \begin{pmatrix} b_n^+ \\ b_n^- \end{pmatrix} \tag{B.8}$$

and

$$\boldsymbol{M}_a \boldsymbol{P}_a(0) \begin{pmatrix} a_{n+1}^+ \\ a_{n+1}^- \end{pmatrix} = \boldsymbol{M}_b \boldsymbol{P}_b(\Lambda) \begin{pmatrix} b_n^+ \\ b_n^- \end{pmatrix} \tag{B.9}$$

where $\boldsymbol{M}_a$ and $\boldsymbol{M}_b$ depend on the light polarization and $\boldsymbol{P}_{a/b}(x)$ refers to the complex exponential matrix evaluated at a given x point. By eliminating $[b_n^+ \; b_n^-]^T$, the field transfer function in a unitary cell is obtained:

$$\begin{pmatrix} a_{n+1}^+ \\ a_{n+1}^- \end{pmatrix} = \boldsymbol{P}_a(0)^{-1}\boldsymbol{M}_a^{-1}\boldsymbol{M}_b\boldsymbol{P}_b(\Lambda)\boldsymbol{P}_b(a)^{-1}\boldsymbol{M}_b^{-1}\boldsymbol{M}_a\boldsymbol{P}_a(a)\begin{pmatrix} a_n^+ \\ a_n^- \end{pmatrix} \tag{B.10}$$

The above expression can be further simplified taken into account the properties of complex exponentials in $\boldsymbol{P}_i(x)$, i.e., $\boldsymbol{P}_i(x)^{-1} = \boldsymbol{P}_i(-x) = \boldsymbol{P}_i^*(x)$. Therefore:

$$\begin{pmatrix} a_{n+1}^+ \\ a_{n+1}^- \end{pmatrix} = \boldsymbol{M}_{ab}\boldsymbol{P}_b(b)\boldsymbol{M}_{ba}\boldsymbol{P}_a(a)\begin{pmatrix} a_n^+ \\ a_n^- \end{pmatrix} \rightarrow \begin{pmatrix} a_{n+1}^+ \\ a_{n+1}^- \end{pmatrix} = \boldsymbol{Q}\begin{pmatrix} a_n^+ \\ a_n^- \end{pmatrix} \tag{B.11}$$

where $\boldsymbol{Q}$ is the so-called translation matrix within a unitary cell. The Q_{ij} terms for E_y-polarized light are:

$$\begin{aligned}
Q_{11} &= e^{-jk_{x,a}a}\left[\cos(k_{x,b}b) - j\frac{1}{2}\left(\frac{k_{x,a}}{k_{x,b}} + \frac{k_{x,b}}{k_{x,a}}\right)\sin(k_{x,b}b)\right] \\
Q_{12} &= e^{jk_{x,a}a}\left[j\frac{1}{2}\left(\frac{k_{x,a}}{k_{x,b}} - \frac{k_{x,b}}{k_{x,a}}\right)\sin(k_{x,b}b)\right] \\
Q_{21} &= e^{-jk_{x,a}a}\left[-j\frac{1}{2}\left(\frac{k_{x,a}}{k_{x,b}} - \frac{k_{x,b}}{k_{x,a}}\right)\sin(k_{x,b}b)\right] \\
Q_{22} &= e^{jk_{x,a}a}\left[\cos(k_{x,b}b) + j\frac{1}{2}\left(\frac{k_{x,a}}{k_{x,b}} + \frac{k_{x,b}}{k_{x,a}}\right)\sin(k_{x,b}b)\right]
\end{aligned} \tag{B.12}$$

whereas for H_y-polarized light are:

$$\begin{aligned}
Q_{11} &= e^{-jk_{x,a}a}\left[\cos(k_{x,b}b) - j\frac{1}{2}\left(\frac{\varepsilon_b k_{x,a}}{\varepsilon_a k_{x,b}} + \frac{\varepsilon_a k_{x,b}}{\varepsilon_b k_{x,a}}\right)\sin(k_{x,b}b)\right] \\
Q_{12} &= e^{jk_{x,a}a}\left[j\frac{1}{2}\left(\frac{\varepsilon_b k_{x,a}}{\varepsilon_a k_{x,b}} - \frac{\varepsilon_a k_{x,b}}{\varepsilon_b k_{x,a}}\right)\sin(k_{x,b}b)\right] \\
Q_{21} &= e^{-jk_{x,a}a}\left[-j\frac{1}{2}\left(\frac{\varepsilon_b k_{x,a}}{\varepsilon_a k_{x,b}} - \frac{\varepsilon_a k_{x,b}}{\varepsilon_b k_{x,a}}\right)\sin(k_{x,b}b)\right] \\
Q_{22} &= e^{jk_{x,a}a}\left[\cos(k_{x,b}b) + j\frac{1}{2}\left(\frac{\varepsilon_b k_{x,a}}{\varepsilon_a k_{x,b}} + \frac{\varepsilon_a k_{x,b}}{\varepsilon_b k_{x,a}}\right)\sin(k_{x,b}b)\right]
\end{aligned} \tag{B.13}$$

Finally, the translation matrix is unimodular, i.e.:

$$Q_{1,1}Q_{2,2} - Q_{2,1}Q_{1,2} = 1. \tag{B.14}$$

On the other hand, due to the periodicity of the structure, the Floquet theorem can be applied. Hence, the problem becomes in an eigenvector and eigenvalue problem:

$$\begin{aligned}
\begin{pmatrix} a_1^+ \\ a_1^- \end{pmatrix} &= e^{-jk_x\Lambda}\begin{pmatrix} a_0^+ \\ a_0^- \end{pmatrix} \\
\boldsymbol{Q}\begin{pmatrix} a_0^+ \\ a_0^- \end{pmatrix} &= e^{-jk_x\Lambda}\begin{pmatrix} a_0^+ \\ a_0^- \end{pmatrix}
\end{aligned} \tag{B.15}$$

The eigenvalue is given by:

$$e^{-jk_x\Lambda} = \frac{1}{2}\left(Q_{1,1} + Q_{2,2}\right) \pm \sqrt{\left[\frac{1}{2}\left(Q_{1,1} + Q_{2,2}\right)\right]^2 - 1} \tag{B.16}$$

and the associated eigenvectors are:

$$\begin{pmatrix} a_0^+ \\ a_0^- \end{pmatrix} = \begin{pmatrix} Q_{1,2} \\ e^{jk_x\Lambda} - Q_{1,1} \end{pmatrix} \text{ and } \begin{pmatrix} e^{jk_x\Lambda} - Q_{2,2} \\ Q_{2,1} \end{pmatrix} \tag{B.17}$$

The eigenvalue equation gives the dispersion-relation equation of the structure, which relates the values of k_z and k_x:

$$\cos(k_x\Lambda) = \frac{1}{2}\left(Q_{1,1} + Q_{2,2}\right) \tag{B.18}$$

The field distribution in the a-layer can be obtained from the previous eigenvector. In order to obtain the eigenvector of the b-layer we can use:

$$\begin{pmatrix} b_0^+ \\ b_0^- \end{pmatrix} = \boldsymbol{P}_b(-a)\boldsymbol{M}_{ba}\boldsymbol{P}_a(a)\begin{pmatrix} a_0^+ \\ a_0^- \end{pmatrix} \tag{B.19}$$

As a result, we have fully described both field distribution, $\phi(x)$, and the associated wavevectors, k_x and k_z, for a periodic two-layer. In the present work, the wave propagates only in the z-axis and thus, $k_x = 0$. For this case, the dispersion-relation equation, i.e., the value of k_z, cannot be solved analytically and numeric root-search methods are required.

Appendix C

Eigenmode Expansion and Mode-Matching

This appendix deals with the eigenmode expansion and mode-matching technique applied to the interface of a homogeneous dielectric medium (Medium I) and one dimensional crosswise subwavelength periodic structure (Medium II). An illustration of this situation for both polarizations is depicted in Fig. C.1, where a plane wave travels from medium I to II.

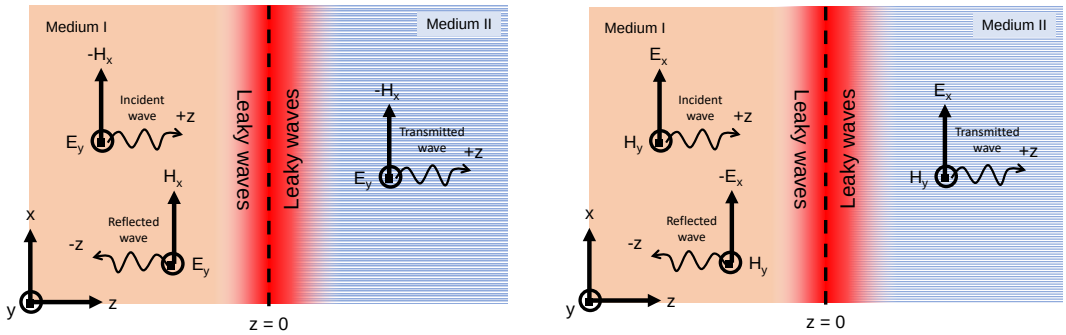

Figure C.1. Illustration of the analysed situation comprised of a natural homogenous dielectric medium (medium I) and a periodic two-layer stack (medium II). Both mediums are semi-infinite in the x- and y-axis. The periodicity of the medium II is along the x-axis. A plane wave is incident from medium I to II with **(a)** TM and **(b)** TM polarization.

Ideally, the number of expanded modes should be ∞, however, computational resources are limited and, from a given point, the contribution of high order modes tends to be negligible. In this work the number of expanded modes has been taken to ensure good convergence. Thus, the number of expanded modes has been truncated up to 50. Furthermore, basing on the results given by these methods, parameters such transmittance and reflectance and the approximation of medium II to a magnetic one are also derived.

C.1 Field Expression in a Homogenous Medium (Medium I)

In a natural homogenous medium Maxwell's equations derived in a plane wave solution being both electric and magnetic components transverse (TEM wave). However, if the field at the interface with a periodic structure is expanded to higher modes then the wave is no longer TEM. Thus, the components of the electric and magnetic fields are:

- TE: $\mathbf{E} = \{E_x, 0, E_z\}$ and $\mathbf{H} = \{0, H_y, 0\}$.
- TM: $\mathbf{E} = \{0, E_y, 0\}$ and $\mathbf{H} = \{H_x, 0, H_z\}$.

where $n_{I,m}$ is the effective refractive index of the m-expanded mode and ε_I the permittivity of the medium I. In a homogeneous medium, the effective refractive index of a plane wave that propagates through the medium ($m = 0$) is equal to the refractive index of the medium. The effective refractive index of leaky modes, i.e., the higher order modes ($m \neq 0$) that do not propagate but can exist at the interface between both media is given by the following dispersion-relation equation:

$$k_{z,m} = \sqrt{k_0^2 \varepsilon_I - \left(k_x + m\frac{2\pi}{\Lambda}\right)^2} \tag{C.1}$$

where Λ stands for the period of medium II, $k_{z,m}$ is the value of the wavevector corresponding to the m-expanded mode, k_0 is the value of the vacuum wavector ($2\pi/\lambda$) and m is an integer number ranging from $-\infty$ to $+\infty$. Taking into account that the incident wave only propagates in the z-axis, $k_x = 0$ and $k_{z,m} = n_{I,m}k_0$. Thus, the effective refractive index can be expressed as:

$$n_{I,m} = \sqrt{\varepsilon_I - \left(m\frac{\lambda}{\Lambda}\right)} \tag{C.2}$$

The values of $n_{I,m}$ are antisymmetric in respect to m, i.e., $n_{I,m} = -n_{I,-m}$. On the other hand, it should be noted that for large λ/Λ relations no diffraction is allow and thus, the effective refractive index becomes imaginary for $m \neq 0$. Therefore, these modes can exist at the interface between the two media but do not propagate.

Finally, the field expressions at the interface ($z = 0$) along the x-axis for the m-mode and both polarizations are summarized in Table C.1 where the term $\phi_m(x)$ is:

$$\phi_m(x) = \int_0^{\Lambda} \exp\left(j\frac{2\pi m}{\Lambda}x\right). \tag{C.3}$$

It has to be noticed, that for $m = 0$ we obtain the typical expression of a plane wave with a constant field along the x-axis, whereas for $m \neq 0$ the field expression corresponding to leaky modes is not constant along the x-axis and these do not propagate.

Table C.1. Field profile expression of the E- and H-fields in medium I.

	TE		TM	
	E	**H**	**E**	**H**
E_x/H_x	$\frac{n_{I,m}}{\varepsilon_I}\phi_m(x)$	–	–	$-n_{I,m}\phi_m(x)$
E_y/H_y	–	$\phi_m(x)$	$\phi_m(x)$	–
E_z/H_z	$-j\frac{k_0}{\varepsilon_I}\frac{d\phi_m(x)}{dx}$	–		$jk_0\frac{d\phi_m(x)}{dx}$

C.2 Field Expression in a Crosswise Periodic Structure (Medium II)

In the second medium comprised by a stack of two-layers, the fields are obtained from solving the dispersion-relation equation of a two-layer periodic medium and TMM using the method explained in Appendix B. Conversely to a homogenous medium, both propagated and leaky waves are not TEM. Thus, the electric and magnetic fields have two components, which are:

- TE: $\mathbf{E} = \{E_x, 0, E_z\}$ and $\mathbf{H} = \{0, H_y, 0\}$.
- TM: $\mathbf{E} = \{0, E_y, 0\}$ and $\mathbf{H} = \{H_x, 0, H_z\}$.

The z-component of the E- and H-field becomes negligible only when $\lambda/\Lambda \to \infty$. Hence, in order to rigorously solve the field between both media, the z-component must be taken into account. By solving the dispersion-relation equation [(Eq. (4.10))], the effective refractive indices for the propagated and leaky modes are obtained. In this case, the equation cannot be solved analytically. Furthermore, the values of $n_{II,m}$ are antisymmetric only for some certain values of m. Hence, the values given when solving the dispersion-equation need to be sorted. The following produce was carried out to assign each value to the associated m-mode:

1. Collect M unsorted imaginary n_{eff} values by solving Eq. (4.10) with a root-finding algorithm, for instance, Newton's method.
2. Calculate the same number of values by using Eq. (C.2) with ε_I equal to the effective permittivity of the two-layers stack.
3. For each value obtained in the first step, compare to those obtained in the second step and assign the corresponding m-position.

Finally, the field expressions (**E** and **H**) of the m-mode for both polarization at the interface are summarised in Table C.2.

Table C.2. Field profile expression of the E- and H-fields in medium II.

	TE		TM	
	E	**H**	**E**	**H**
E_x/H_x	$\frac{n_{II,m}}{\varepsilon_{II}(x)}\phi_x(x)$	–	–	$-n_{I,m}\phi_x(x)$
E_y/H_y	–	$\phi_m(x)$	$\phi_m(x)$	–
E_z/H_z	$-j\frac{k_0}{\varepsilon_{II}(x)}\frac{d\phi_m(x)}{dx}$	–	–	$jk_0\frac{d\phi_m(x)}{dx}$

C.3 Interface between Medium I and II

Once the propagation constants and field profiles have been calculated in both medium, amplitude of each expanded mode is obtained by applying the so-called mode-matching technique. The relation is given by the transmitted and reflected vectors containing the amplitude of each mode and applying boundary conditions. For the sake of simplicity, this is done at $z = 0$ in order to eliminate the complex exponential of the field. Therefore, after some cumbersome process it can be arrived to Eqs. C.4 and C.5 for E_y-polarised light. Similar expression can be obtained for H_y-polarised light [Eqs. (C.6) and (C.7)].

$$\boldsymbol{a} + \boldsymbol{r} = \boldsymbol{V_{II}}\boldsymbol{t} \tag{C.4}$$

$$\boldsymbol{Y_I}(\boldsymbol{a} - \boldsymbol{r}) = \boldsymbol{V_{II}}\boldsymbol{Y_{II}}\boldsymbol{t} \tag{C.5}$$

$$\boldsymbol{a} + \boldsymbol{r} = \boldsymbol{U_{II}}\boldsymbol{t} \tag{C.6}$$

$$\boldsymbol{Z_I}(\boldsymbol{a} - \boldsymbol{r}) = \boldsymbol{V_{II}}\boldsymbol{t} \tag{C.7}$$

The terms $\boldsymbol{a}$, $\boldsymbol{r}$ and $\boldsymbol{t}$ stand for arrays that contains the complex amplitudes of the incident (medium I), reflected (medium I) and transmitted (medium II) modes. The size of these arrays is $N \times 1$, where N is the number of expanded modes. $\boldsymbol{Y_I}$ and $\boldsymbol{Y_{II}}$ stand for the diagonal admittance matrices in the medium I and II, respectively, and equal to $\boldsymbol{Y_I} = n_{I,m}\boldsymbol{I}$ and $\boldsymbol{Y_{II}} = n_{II,m}\boldsymbol{I}$, where $\boldsymbol{I}$ is the unitary matrix. $\boldsymbol{Z_I}$ is the impedance matrix of medium I, which is defined as $\boldsymbol{Z_I} = n_{I,m}/\varepsilon_I\boldsymbol{I}$. Finally, the terms $\boldsymbol{V_{II}}$ and $\boldsymbol{U_{II}}$ are the matrices whose columns contain the eigenvector of the m-mode of the E- and H-field, respectively, in the medium II. The eigenvectors are calculated as:

$$V_{II}(m,p) = \int_0^{\Lambda} E_{II,m}(x)\exp\left(j\frac{2\pi p}{\Lambda}x\right)dx \tag{C.8}$$

and

$$U_{II}(m,p) = \int_0^{\Lambda} H_{II,m}(x)\exp\left(j\frac{2\pi p}{\Lambda}x\right)dx \tag{C.9}$$

where $E_{II,m}(x)$ and $H_{II,m}(x)$ are the y-component of the E- and H-field, respectively, in the periodic medium and p is an integer number that ranges between $-N/2$ and $N/2$.

Here, only a plane wave impinges from the medium I into the II. Therefore, the array $\boldsymbol{a}$ equals 1 for $m = 0$ and 0 for $m \neq 0$. The value of the transmission and reflection arrays

is calculated using Eqs. (C.10) and (C.11) for the E_y-polarised light and using Eqs. (C.12) and (C.12) for H_y-polarised light.

$$\boldsymbol{t} = 2\left(\boldsymbol{I} + \boldsymbol{V_{II}}^{-1}\boldsymbol{Y_I}^{-1}\boldsymbol{V_{II}}\boldsymbol{Y_{II}}\right)^{-1}\boldsymbol{V_{II}}\boldsymbol{a} \tag{C.10}$$

$$\boldsymbol{r} = \boldsymbol{V_{II}}\boldsymbol{t} - \boldsymbol{a} \tag{C.11}$$

$$\boldsymbol{t} = 2\left(\boldsymbol{I} + \boldsymbol{U_{II}}^{-1}\boldsymbol{Z_I}^{-1}\boldsymbol{V_{II}}\right)^{-1}\boldsymbol{U_{II}}\boldsymbol{a} \tag{C.12}$$

$$\boldsymbol{r} = \boldsymbol{U_{II}}\boldsymbol{t} - \boldsymbol{a} \tag{C.13}$$

Once the values of $\boldsymbol{r}$ and $\boldsymbol{t}$ are obtained, the E- and H-fields in the x-z plane of both medium can be calculated as:

$$E_I(x,z) = \sum_m (a_m \pm r_m) E_{I,m}(x) \exp\left(jk_0 n_{I,m} z\right) \tag{C.14}$$

$$H_I(x,z) = \sum_m (a_m \pm r_m) H_{I,m}(x) \exp\left(jk_0 n_{I,m} z\right) \tag{C.15}$$

$$E_{II}(x,z) = \sum_m t_m E_{II,m}(x) \exp\left(-jk_0 n_{II,m} z\right) \tag{C.16}$$

$$H_{II}(x,z) = \sum_m t_m E_{II,m}(x) \exp\left(-jk_0 n_{II,m} z\right) \tag{C.17}$$

where the sign of $\pm$ in the field expression of medium I will depend on the polarization.

C.4 Reflectance and Transmittance

Power

The power, P, can be defined as the integral of the Poynting vector over a line, region or volume. The Poynting vector is defined as $\boldsymbol{S} = \Re(\boldsymbol{E} \times \boldsymbol{H}^*)$. For our case, the Poynting vector for an E_y- and H_y-polarized light is given by Eqs. (C.18) and (C.19), respectively.

$$\boldsymbol{S} = S_x\hat{\boldsymbol{x}} + S_z\hat{\boldsymbol{z}} = \Re(E_y H_z^*\hat{\boldsymbol{x}} - E_y H_x^*\hat{\boldsymbol{z}}) \tag{C.18}$$

$$\boldsymbol{S} = S_x\hat{\boldsymbol{x}} + S_z\hat{\boldsymbol{z}} = \Re(-E_z H_y^*\hat{\boldsymbol{x}} + E_x H_y^*\hat{\boldsymbol{z}}) \tag{C.19}$$

The electric and magnetic fields at $z = 0$ vary only in the x-axis. The integral of $\boldsymbol{S}$ gives a vector with the amount of power in each direction, i.e.:

$$\boldsymbol{P} = \int \boldsymbol{S}dx = \int S_x dx\hat{\boldsymbol{x}} + \int S_z dx\hat{\boldsymbol{z}} = P_x\hat{\boldsymbol{x}} + P_z\hat{\boldsymbol{z}} \tag{C.20}$$

Reflectance

Reflectance, R, is the relation between the reflected power of the m-mode, $P_{r,m}$ and the incident power, P_i, which typically corresponds to $m = 0$. Both powers are in the medium I, thus we have:

$$R_m = \frac{P_{r,m}}{P_i} = \frac{\left(P_{r,m,x}^2 + P_{r,m,z}^2\right)^{1/2}}{|P_{0,z}|} \tag{C.21}$$

where $P_{r,m,x}$ and $P_{r,m,z}$ are x- and z-components of power of the reflected m-mode and $P_{0,z}$ the z-component of the incident power ($m = 0$). The reflected powers can be defined as:

$$P_{r,m,x} = |r_m|^2 P_{m,x} \tag{C.22}$$

$$P_{r,m,z} = |r_m|^2 P_{m,z} \tag{C.23}$$

Hence, we arrive to the following expression:

$$R_m = |r_m|^2 \frac{\left(P_{m,x}^2 + P_{m,z}^2\right)^{1/2}}{|P_{0,z}|} \tag{C.24}$$

where the values $P_{m,x}$ and $P_{m,z}$ are obtained from the expanded fields and using the aforementioned definitions of power.

Transmittance

Transmittance, T, is the relation between the transmitted power of the m-mode, $P_{t,m}$, and the incident power, P_i. The transmitted power is in medium II, whereas incident power in medium I. Hence, we have an expression similar to the reflectance:

$$T_m = \frac{P_{t,m}^{II}}{P_i} = \frac{\left(P_{t,m,x}^{II\ 2} + P_{t,m,z}^{II\ 2}\right)^{1/2}}{|P_{0,z}|} \tag{C.25}$$

The x- and z-component of the transmitted power for each m-mode in the medium II can be defined as:

$$P_{t,m,x} = |t_m|^2 P_{m,x}^{II} \tag{C.26}$$

$$P_{t,m,z} = |t_m|^2 P_{m,z}^{II} \tag{C.27}$$

Hence, the following expression is obtained:

$$T_m = |t_m|^2 \frac{\left(P_{m,x}^{II\ 2} + P_{m,z}^{II\ 2}\right)^{1/2}}{|P_{0,z}|} \tag{C.28}$$

where the values $P_{m,x}^{II}$ and $P_{m,z}^{II}$ are obtained from the expanded fields and using the aforementioned definitions of power.

C.4.1 Fresnel Equations

The reflection, r, and transmission, t, coefficients between two homogenous media and assuming normal incidence of the light to the interface are given by Eqs. (C.29) - (C.31), which are the so-called Fresnel equations.

$$r(E_y) = \frac{Y_{II} - Y_I}{Y_I + Y_{II}} \tag{C.29}$$

$$r(H_y) = \frac{Y_I - Y_{II}}{Y_I + Y_{II}} \tag{C.30}$$

$$t = \frac{2Y_I}{Y_I + Y_{II}} \tag{C.31}$$

The parameter Y stands for the normalized admittance of the medium I or II, and is defined as:

$$Y = \sqrt{\frac{\varepsilon_r}{\mu_r}} \tag{C.32}$$

Finally, the reflectance and transmittance are $|r|^2$ and $\frac{Y_{II}}{Y_I}|t|^2$, respectively.

C.4.2 Crosswise Subwavelength Periodic Structure as a Homogenous Medium with Magnetic Properties

A crosswise subwavelength periodic dielectric structure –not in the deep-subwavelength regime– exhibits an effective refractive index given by the dispersion-relation equation but does not behave as a pure homogeneous dielectric material since the equivalent impedance cannot be expressed only in terms of $1/n_{equiv}$. In order to fulfil both characteristics, the equivalent medium needs to have some magnetic response, i.e., $\mu_r \neq 1$. If the power is not transferred to leaky modes and assuming that the equivalent permittivity and permeability are positive and real, then these can be obtained from the following equations:

$$n_{equiv} = \sqrt{\mu_{r,II}\varepsilon_{r,II}} \tag{C.33}$$

$$T_0 = \frac{Y_{II}}{Y_I}\frac{4Y_I^2}{Y_I^2 + 2Y_IY_{II} + Y_{II}^2} \tag{C.34}$$

in which after doing some manipulations it can be arrived to:

$$Y_{II} = \frac{2 \pm \sqrt{Y_I^2 - Y_I^2T_0} - T_0Y_I + 2Y_I}{T_0} \tag{C.35}$$

$$\mu_{r,II} = \frac{n_{equiv}}{Y_{II}} \tag{C.36}$$

$$\varepsilon_{r,II} = n_{equiv}Y_{II} \tag{C.37}$$

assuming that the medium I is purely dielectric and the sign in Eq. (C.35) is determined if n_I is greater $(-)$ or lower $(+)$ than n_{equiv}.